

Kinematics and Kinetics of an In-Parallel-Actuated Soft Manipulator *

Olalekan Ogunmolu

Perelman School of Medicine
The University of Pennsylvania
Philadelphia, PA 19104, USA.
ogunmolo@pennmedicine.upenn.edu

James Pikul

Mechanical Engineering,
The University of Pennsylvania
Philadelphia, PA 19104, USA.
pikul@seas.upenn.edu

Rodney D. Wiersma

Perelman School of Medicine
The University of Pennsylvania
Philadelphia, PA 19104, USA.
wiersmr@pennmedicine.upenn.edu

A soft parallel multi-degree of freedom robot is here put forward to counterbalance the present preoccupation with in-parallel-actuated rigid mechanisms, currently prevalent in precision manipulation tasks. We study the kinematics of the entirely soft mechanism using continuum mechanics and differential geometry. We then derive the Newton-Euler system of equations using elasticity theory. Relating the solutions to the dynamic boundary value problem of the soft actuators' total Cauchy stress tensor to the force wrenches on the object/load, we write out the manipulation map and construct the associated Jacobian for its direct positioning analysis. Within the bounds here set, the mechanism is intended to provide precise manipulation in lieu of the rigid parallel platforms that are used today. Our goal is to edge open the door a little further towards in-parallel soft actuation mechanisms that provide an equivalent or better manipulation precision as well as compliance needed for sensitive medical application tasks.

1 INTRODUCTION

We present the systematic analysis of an in-parallel-actuated soft continuum manipulator for use in clinical radiation therapy. Possible applications could be the real-time closed-loop automatic motion deviation correction, particularly during beam-on time, in robotic radiosurgery; or as a magnetic resonance imaging (MRI)-compatible soft robotic patient motion correction system in frameless and maskless robot-based cranial manipulation systems [1, 2]. It may hasten the current treatment time in clinics, minimize patient discomfort post-treatment (as opposed to rigid frames and masks currently used in frame and mask-based RT), or drastically improve

the dose efficacy so that the patient's treatment can be effectively fractionated. Other applications are in the animation industry where animated pluses are required to be accurately actuated to specific configurations [3, 4] or the real-time control of hyperelastic materials [5, 6].

Contributions: We present parallel multi-degree of freedom soft system made out of deformable shells. The individual shells are constrained to strain along the circumferential direction and their kinematic arrangement have actuation freedoms [7] that constrain yield the desired range of motions for the complete manipulation of an object located in their workspace.

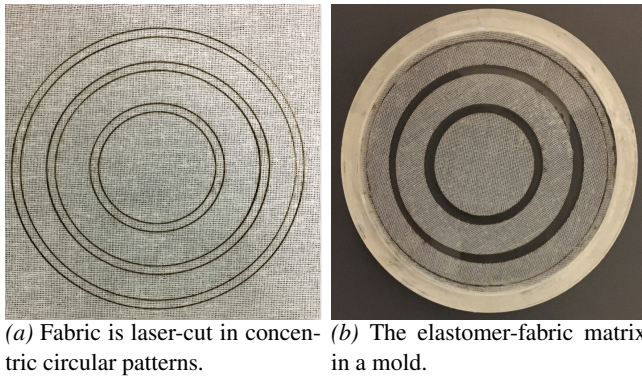
We first provide a constitutive model that governs their deformation given the baked deformation constraints into the material properties of the individual actuators. We then analyze the kinematics and kinetics of the mechanism with the minimal number of linkages that achieves 6-DOF manipulability.

Iterating from [2, 8–12], we expand upon the kinematics and dynamics of the multi-DOF soft actuation system. The rest of this paper is organized as follows: in § 3, we review the hardware setup and system configuration, prescribe the finite elastic deformation model and solve the dynamic boundary value problem. We then analyze the contact kinematics with the head in § 4 and derive the dynamic equations in § 5. In § 6, we derive the end-effector velocities and forces; and conclude the paper in § 8. Proofs and derivations are provided in the appendices.

2 Mechanisms Description

Inspired by the behavior of the skin papillae of certain cephalopods (bivalves, mollusks, octopus and cuttlefish) which can change their planar and smooth physical texture

*The research reported in this publication was supported by National Cancer Institute of the National Institutes of Health under award number R01CA227124.



(a) Fabric is laser-cut in concentric circular patterns. (b) The elastomer-fabric matrix in a mold.

Fig. 1: Actuators fabrication

into 3D textures up to a specific maximum size [13] in less than 3 seconds [14], we pattern the design of our soft actuators similar to the skin papillae of these organisms where the elasticity of the skin papillae is controlled by a muscular hydrostatic mechanism: an elastomeric dermis antagonizes the muscle’s fibers – causing uniaxial shape erection.

2.1 Soft Actuator Design

The soft actuator fabrication methodology is illustrated in Fig. 1. A thin-layered fabric is laser cut into circular patterns (a), the cut meshes are removed and laid onto uncured silicone (b) which has been poured into a mold (cast with soft lithography) [15]. We further add a silicone topcoat layer to the fabric before we allow it to cure. Upon low pneumatic pressurization, the cured rubber deforms, obeying a Circumferentially-COnstrained And Radially Stretched fiber-Elastomer (CCOARSE) property [16] as seen in Fig. 2a. This unique deformation pattern is similar to the way a balloon would stretch along its axial direction if a rope were tied around its circumference. The soft actuator, after cure, is laid onto an impact-resistant, low-temperature rigid PVC insulation foam sheet, encased in a carbon nanofiber material (Fig. 2b). This aids radiation transparency, an important requirement in robotic radiation therapy and stereotactic radiosurgery [17] where the immobilization mechanism must not attenuate dose radiation. The actuator has shells with radii $2.75 \pm 0.5\text{cm}$ and $3.0 \pm 0.5\text{cm}$ respectively and there exists constant volume within their wall. The wall thickness is 0.25cm in the reference configuration, to accommodate flex and shrinking from repeated use as well as exhibit enough tensile strength for robust manipulation. This proposed fabrication method allows users to rapidly iterate different designs with compressed low air pressure (at 3-15 psi) which is advantageous because air is (i) cheaply available, (ii) environmentally-friendly, (iii) avoids electrical wirings, (iv) lightweight, and (v) inviscid. This aids a clean and safe human-robot workspace suitable for medical robotics applications such as in emerging magnetic resonance imaging-linear accelerators (MRI-Linacs) [18–20].

We fabricate the IAB’s elastic membranes from elastomeric rubber with a shore hardness of 10A (Dragon Skin 10, Smooth-on Inc.) and 475 psi tensile strength. We control the circumferential strain with concentric circular fabric

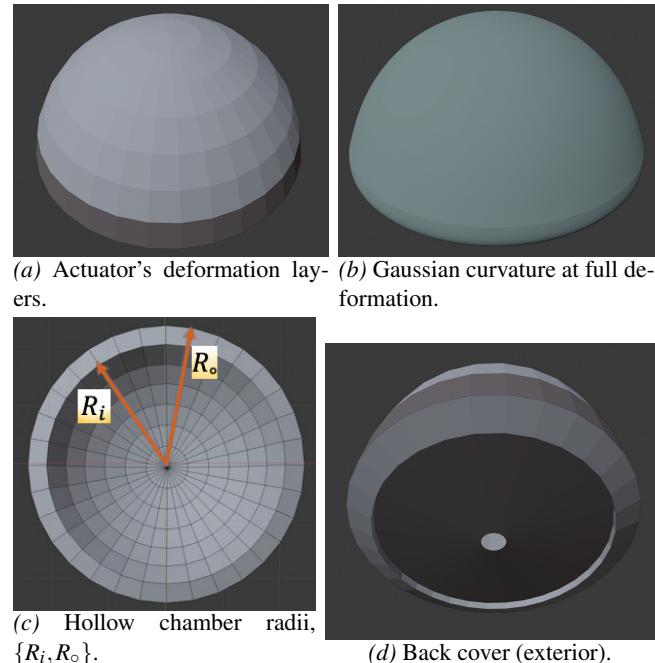


Fig. 2: IAB Geometrical Model

meshes (Fleishman Fabrics & Supplies, Philadelphia, PA) similar to some of the designs of [14, 16]. Deformation can be sensed with electrical grade Kapton polyimide sheets cut into specific kirigami geometries as proposed in [21] or [22]. Furthermore, inspired by the innervated fins of cuttlefish which allow their mechano-receptors to process tactile information from their immediate surroundings, we integrate Kirigami sensors, made out of electrical-grade Kapton Polyimide onto the actuators’ skin to gather cues for required specific deformations [23]. We then use plasma bonding to join the kirigami layers with the actuators’ surface using a hand-held, atmospheric corona treater (from Electro-Technic Products) [22, 24]. The corona treated sensor is firmly pressed against the cured rubber and left undisturbed for 24 hours at room temperature after which Kapton layer is laid over the actuators.

In their reference configuration, the actuators are planar while in the current configuration, they deform, creating an internal cavity that contributes a single degree of freedom (DOF) to a soft actuator linkage in the system – in part holding the object in place and moving the head along a desired axis of motion. To enforce the single DOF during deformation, a fabric material was laser-cut in concentric circular patterns (Fig. 1a). Uncured silicone (with equal parts of Dragon Skin A and B) are then mixed, degassed at 29in Hg, and then poured into a mold (additively manufactured). We further laid the cut fabric membrane onto the uncured rubber, add silicone topcoat and the admixture was allowed to cure at room temperature. After room-temperature vulcanization, we post-cured the admixture at 176°F for 2 hours and at 212°F for 1 hour respectively in order to allow the rubber material to attain its maximum physical properties. Each IAB is linked to the object – each supporting only a part of the total load, redistributing link-loads and solving some of the problems with serial links. Inspired by [16], the

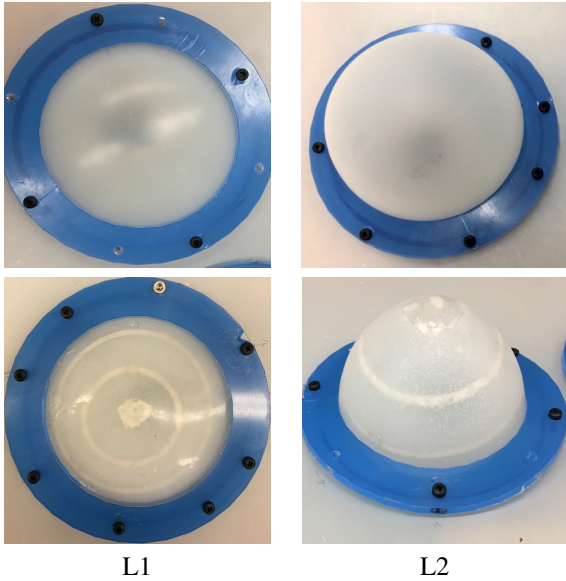


Fig. 3: Deformation of Elastomer-only (top) and Elastomeric-Fabric Matrix (bottom) under Low Air Pressurization (3-15psi).

soft robot chambers are constrained to deform only along the radial strain in order to exert appropriate push on an object.

The experiments of Fig. 3 illustrates the deformation behavior of the manufactured actuator with two different designs. The cured rubber material is screwed onto a bottom PVC foam sheet using **nylon** Phillips screws on a laser-cut acrylic ring. The behavior at different levels of pressurization are indicated in each column of the figure. The top row shows the cured silicone without fabric while the bottom row shows the cured elastomer with the entrenched fiber matrix. As seen, the fiber-free material exhibits a circumferential strain as well as radial strain while the fiber-constrained elastomer exhibits a radial strain only. We are able to generate a full *Gaussian deformation* and return to the reference planar configuration in 3 second (see more images and videos in scriptedonachip.com/soro) similar to the spikes produced by the skin papillae of the Octopus. These quick Gaussian spikes are useful for rapid manipulation, grasp, push and release of objects when the actuators are interconnected as linkages to fit a kinematician's desired mechanisms. For example, the soft compliance and tensile strength of this silicone material make it well-suited for treatment procedures where non-magnetic and radiation-transparent components can boost stereotactic precision as well as improve tumor control in MRI-LINACs. We find these material properties make the robot soft enough for patient comfort yet strong enough to withstand extremely nonlinear deformation from head forces in patient motion correction. Together with the layered composition during fabrication, the robot is resistant to puncture, wear and tear (given their shrinkage of $< 0.001\text{in./in.}$), and they generally preserve the CCOARSE property even in contact with a typical adult head weight of 55 – 66kg [25–27] upon air pressurization. The actuator was cast to be 3 – 5mm thick (see Fig. 3). The ingrained fabric membrane within the elastomer imposes the

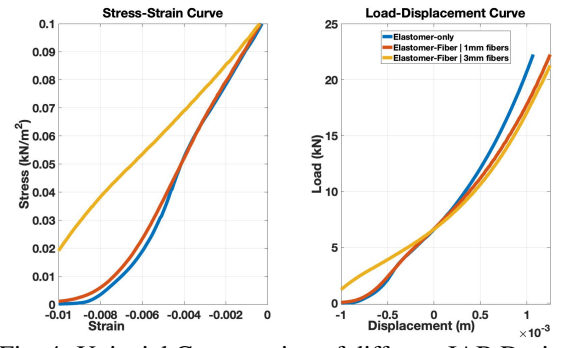


Fig. 4: Uniaxial Compression of different IAB Designs.

CCOARSE property, constraining the circumferential expansion of the rubber and exerting a radially symmetric stretch as shown in the bottom row of Fig. 3.

In Fig. 4, we test the material properties of the elastomer-only actuator, as well as the elastomer-fiber matrix model. Two types of fiber cross-sections are considered: a 0.5mm and a 1mm thick circular fibers engraved within the elastomer. We applied uniaxial compression forces of up to 20kN using a tensile testing machine (MTS Criterion Electromechanical Universal Test System, Model 43), generating compression forces which produce 0.5mm displacement per min. As seen in the figure, the IAB exhibits mostly linear elastic properties under uniaxial loading. We also notice that the presence of the fiber increases the material's young's modulus. Physically, this improves the deformation properties of the material when in contact with an object, essentially enforcing radially symmetric, yet circumferentially-constrained deformation. The more the layers of the fiber or the thicker the fiber layers, the better the actuator preserves the CCOARSE property during deformation or when in contact with traction forces.

2.2 Example Mechanism Setup

We test a mechanism meant for head motion correction in medical applications such as magnetic resonance imaging or emerging MRI-Linac applications. Explorative robotic positioning research studies have demonstrated the feasibility of maintaining stable patient cranial motion consistent with treatment plans using rigid Stewart-Gough platforms [28–30]. These achieve a $\leq 0.5\text{mm}$ and $\leq 0.5^\circ$ positioning accuracy 90% of the time. While aiding better clinical accuracy, they utilize rigid metallic components, electric motors and linear actuators which are not suitable for MRI imaging: they interfere with the magnets of the MRI machine and can lead to patient fatality or significant damage to the MRI machine [31]. Time-resolved MRI techniques, which provide superior soft tissues image scans, should be able to provide soft tissues delineation for use in brain or head and neck (H&N) radiation therapy (RT). Existing frame-based and frameless and maskless robotic motion correction mechanisms are not suitable for this because of their electro-mechanical parts that introduce serious safety concerns.

We position eight IABs around the patient's cranium as illustrated in Fig. 5. The IABs are held in place around the

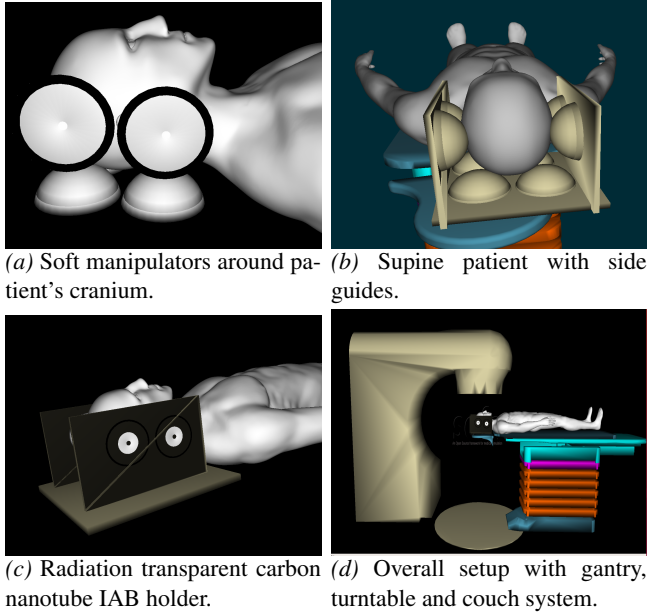


Fig. 5: System setup.

head by a low-temperature rigid PVC foam insulation sheet, encased in carbon fiber to prevent radiation beam attenuation. Velcro stickers (not shown) hold the IABs in place. The freedoms provided by each IAB within the setup in Fig. 5b are described as follows: the side actuators correct head motion along the *left-right* axis of the head anatomy, including the yaw and roll motions, while the base IABs correct the head motion along the *anterior-posterior* axis [7, Ch. 2]. This arrangement offers prehensile manipulation via sensor-based motion manipulation strategies with flexible and electroelastic proprioceptive sensor plans [21,22,32,33]. By this, we mean the mechanical interactions of pushing or releasing by the IABs may be harnessed to further improve head manipulation robustness [34–36].

3 Deformation Analysis

Suppose that at rest, the IAB occupies a stress-free reference configuration \mathcal{B}_0 with boundary $\delta\mathcal{B}_0$ when no mechanical loads or electric fields within the sensor are present. Upon the application of a mechanical load and an electric field, deformation occurs so that the body is transformed into a new configuration \mathcal{B} with boundary $\delta\mathcal{B}$. Material points in \mathcal{B}_0 are denoted by position vectors \mathbf{X} and they have a correspondence in configuration \mathcal{B} of \mathbf{x} . We assume regularity in the deformation from \mathcal{B}_0 to \mathcal{B} , denoted by χ such that $\mathbf{x} = \chi(\mathbf{X}, t)$. In the Lagrangean configuration, we define the deformation tensor to be $\mathbf{F} = \text{Grad } \chi$ with Grad being the gradient operator acting on the material points, \mathbf{X} , in the configuration \mathcal{B}_0 . The common notations throughout the rest of this article are as defined in Table 1. We work from a continuum mechanics framework, whereby we consider only final configurations of the soft actuators; thus we drop the explicit dependence of a configuration on time and rather write it as $\chi(\mathbf{X})$.

Table 1: Common Notations in Article

Notation	Definition
B	An open set of particles on a Body, B
\mathbf{F}	The deformation gradient tensor, $\mathbf{F} = \nabla \chi_k(\mathbf{X}) = \dot{\chi}_k(\mathbf{X})$.
$\boldsymbol{\sigma}$	The Cauchy stress tensor.
\mathbf{C}	The right Cauchy-Green tensor, $\mathbf{C} = \mathbf{F}^T \mathbf{F}$.
\mathbf{B}	The left Cauchy-Green tensor, $\mathbf{B} = \mathbf{F} \mathbf{F}^T$.
$\mathbf{v}(\mathbf{x})$	The velocity field $\dot{\chi}(\mathbf{x}) = \dot{\chi}(\chi^{-1}(\mathbf{X}))$, where without loss of generality, we have taken $X = \mathbf{X}$, i.e. the place of X .

3.1 Nonlinear Elastic Deformation Model

As we are dealing with fluids in the chambers of the IABs, *we use the Eulerian specification in our stress field equations*. Forces that produce deformations are derived using the strain energy-invariants relationship. For readers implementing these principles on solids or hyperelastic materials, a Lagrangean formulation may be appropriate since a reference configuration may be chosen to coincide with the geometry of the solid initially.

Circular fibers are embedded within the elastomeric IAB volume as a reinforcement for conformal radially symmetric deformation, and the elastic properties of the elastomer and fiber reinforcing are described in terms of the strain-energy functions Ψ_{iso} and Ψ_{mesh} respectively. Choosing a Mooney-Rivlin formulation [37,38], we let the elastomer energy, Ψ_{iso} , depends on the invariants I_1 , and I_2 which are functions of the principal stretches, $\lambda_r, \lambda_\phi, \lambda_\theta$ i.e.,

$$I_1 = \text{tr}(\mathbf{C}) = \lambda_r^2 + \lambda_\phi^2 + \lambda_\theta^2, \quad \text{and} \\ I_2 = \text{tr}(\mathbf{C}^{-1}) = \lambda_r^{-2} + \lambda_\phi^{-2} + \lambda_\theta^{-2}, \quad (1)$$

where $\lambda_r \lambda_\phi \lambda_\theta = 1$ following the incompressibility assumption of the elastomeric IAB material. The Mooney-Rivlin strain energy for small deformations as a function of the strain invariants of (1) is

$$\Psi_{\text{iso}}(I_1, I_2) = \frac{1}{2} C_1(I_1 - 3) + \frac{1}{2} C_2(I_2 - 3). \quad (2)$$

The fiber membrane's strain energy is constrained along the circumferential direction \mathbf{M} so that it only applies along the radial, r , and zenith, ϕ , axes (see Fig. 6). We set the strain

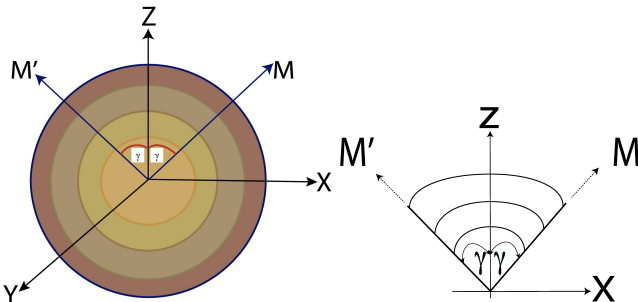


Fig. 6: Sketch of an IAB strip reinforced by radially symmetric circular membranes at angles, γ , along directions \mathbf{M} and \mathbf{M}' .

energy invariant as $I_4 = \mathbf{M} \cdot \mathbf{CM}$, where the symbol “.” denotes the dot product and we choose the standard reinforcing model *i.e.*,

$$\Psi_{\text{mesh}}(I_4) = \frac{C_4}{2}(I_4 - 1)^2 \quad (3)$$

where C_4 is the fiber stiffness. We consider the material to be incompressible ($J \equiv \det \mathbf{F} = 1$) with the total energy of the elastomer-fiber composite being

$$\Psi(I_1, I_2, I_4) = \Psi_{\text{iso}}(I_1, I_2) + \Psi_{\text{mesh}}(I_4). \quad (4)$$

To find a closed-form expression for I_4 , we consider a strip of the IAB material in the XY plane with vectors \mathbf{M} in the reference configuration forming circular segments with angles γ as shown in Fig. 6. The matrix forms of \mathbf{M} and \mathbf{M}' are

$$\mathbf{M} = [\cos \gamma, \sin \gamma, 0]^T, \mathbf{M}' = [\cos \gamma, -\sin \gamma, 0]^T. \quad (5)$$

The anisotropy term is only active if $I_4 > 1$ so that the matrix bears the stress under compression in the fiber direction. If there is a deformation, we must have

$$\mathbf{m} = \mathbf{FM} = \begin{bmatrix} \lambda_r \cos \gamma & \lambda_\phi \sin \gamma & 0 \end{bmatrix}^T \quad (6)$$

where λ_r and λ_ϕ are the principal stretches along the axial and zenith directions, respectively. The fiber invariant is,

$$I_4 = \mathbf{M} \cdot \mathbf{CM} = \left[\lambda_r^2 \cos^2 \gamma, \lambda_\phi^2 \sin^2 \gamma, 0 \right]^T \quad (7)$$

and by symmetry we have $\mathbf{M}' \cdot \mathbf{CM}' = I_4$.

3.2 Strain Analysis: The Deformation Gradient

Since the physical texture of the deformed IAB material is a hemisphere, we choose spherical polar coordinates (r, ϕ, θ) , where r represents the radial distance of the particle from

a fixed origin, θ is the azimuth angle on a reference plane through the origin and orthogonal to the polar angle, ϕ . Denote the internal and external radii as r_i , and r_o respectively with current/reference configuration constraints (since radial symmetry is preserved throughout deformation as seen in Fig. 7),

$$\begin{aligned} r_i \leq r \leq r_o, \quad 0 \leq \theta \leq 2\pi, \quad 0 \leq \phi \leq \pi/2 \\ R_i \leq R \leq R_o, \quad 0 \leq \Theta \leq 2\pi, \quad 0 \leq \Phi \leq \pi/2. \end{aligned} \quad (8)$$

The position vectors \mathbf{R} and \mathbf{r} in either configurations are

$$\mathbf{R} = \begin{pmatrix} R \cos \Theta \sin \Phi, \\ R \sin \Theta \sin \Phi, \\ R \cos \Phi \end{pmatrix} \mathbf{r} = \begin{pmatrix} r \cos \theta \sin \phi, \\ r \sin \theta \sin \phi, \\ r \cos \phi \end{pmatrix}. \quad (9)$$

Given the incompressibility of the IAB material, the material volume contained between the IAB walls (of radii R_o and R_i respectively) remains constant throughout deformation, *i.e.* $\frac{2}{3}\pi(R^3 - R_i^3)$ being equal in volume to $\frac{2}{3}\pi(r^3 - r_i^3)$ so that

$$r^3 = R^3 + r_i^3 - R_i^3, \quad \theta = \Theta, \quad \phi = \Phi. \quad (10)$$

For bases $\{\mathbf{e}_x\}$ and $\{\mathbf{e}_X\}$ (with respect to an observer) in the current and reference configurations respectively, we introduce the gradient operator, ∇ , (in the Lagrangean axes) for a fiber element $\mathbf{dx} = \mathbf{dx}_r \mathbf{e}_r + \mathbf{dx}_\phi \mathbf{e}_\phi + \mathbf{dx}_\theta \mathbf{e}_\theta$ (in Eulerian axes) so that

$$\nabla = \mathbf{e}_R \frac{\partial}{\partial R} + \mathbf{e}_\Phi \frac{1}{R} \frac{\partial}{\partial \Phi} + \mathbf{e}_\Theta \frac{1}{R \sin \Phi} \frac{\partial}{\partial \Theta}. \quad (11)$$

The deformation gradient, \mathbf{F} , as a dyadic product of a material line element in the current configuration and the gradient operator (11) is

$$\begin{aligned} \mathbf{F} &= \mathbf{dx} \otimes \nabla \\ &= (\mathbf{dx}_r \mathbf{e}_r + \mathbf{dx}_\phi \mathbf{e}_\phi + \mathbf{dx}_\theta \mathbf{e}_\theta) \otimes \\ &\quad \left(\mathbf{e}_R \frac{\partial}{\partial R} + \mathbf{e}_\Phi \frac{1}{R} \frac{\partial}{\partial \Phi} + \mathbf{e}_\Theta \frac{1}{R \sin \Phi} \frac{\partial}{\partial \Theta} \right) \end{aligned} \quad (12)$$

where \otimes denotes the dyadic product between two tensor fields. We can verify that the following deformation gradient relation holds (using (10) as a representative configuration

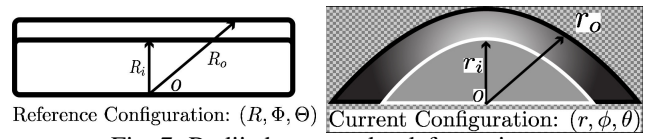


Fig. 7: Radii change under deformation.

changes relation)

$$\mathbf{F} = \begin{pmatrix} \frac{R^2}{r^2} & -\frac{\phi}{R} & -\frac{\theta}{R} \\ 0 & \frac{r}{R} + \frac{1}{R} & -\frac{\theta}{R} \cot\phi \\ 0 & 0 & \frac{r}{R} + \frac{\phi}{R} \cot\phi + \frac{1}{R \sin\Phi} \end{pmatrix} \quad (13)$$

(see Appendix A for the derivation). Given the fiber constraints along the θ direction, the deformation gradient actually turns out to be

$$\mathbf{F} = \begin{pmatrix} \frac{R^2}{r^2} & -\frac{\phi}{R} & 0 \\ 0 & \frac{r}{R} + \frac{1}{R} & 0 \\ 0 & 0 & 1 \end{pmatrix} \quad (14)$$

with principal stretches,

$$\lambda_r = \frac{R^2}{r^2}; \quad \lambda_\phi = \frac{r}{R} + \frac{1}{R}; \quad \lambda_\theta = 1 \quad (15)$$

and associated right and left Cauchy-Green tensors

$$\mathbf{C} = \mathbf{B} = \begin{pmatrix} \frac{R^4}{r^4} & 0 & 0 \\ 0 & \left(\frac{1}{R} + \frac{r}{R}\right)^2 & 0 \\ 0 & 0 & 1 \end{pmatrix}. \quad (16)$$

3.3 Macroscopic Representation of Deformation

At a material point \mathbf{X} of the IAB surface in a configuration \mathcal{B} , it can be verified that the tensor $\mathbf{C} - \mathbf{I}$ represents a change in length of an arbitrary line element of the material. For the material not to be strained, we must have the Lagrangean strain tensor (strain rate) as zero *i.e.* $\mathbf{E} = \frac{1}{2}(\mathbf{C} - \mathbf{I}) = 0$. A particle \mathbf{X} 's displacement from the reference to the current configurations must be such that the point difference $d = \mathbf{x} - \mathbf{X}$ is $d(\mathbf{X}) = \chi(\mathbf{X}) - \mathbf{X}$, where $\chi(\mathbf{X})$ follows the notations of [1, 2, 40]. We therefore characterize the point differences by the two-point *displacement gradient*,

$$\mathbf{D} = \text{Grad } d(\mathbf{X}) = \mathbf{F} - \mathbf{I}. \quad (17)$$

For the unit vectors \mathbf{m} and \mathbf{M} for material line elements \mathbf{dx} and \mathbf{dX} in the current and reference configurations respectively¹, it follows from the invariant of deformation that

$$\mathbf{m}|\mathbf{dx}| = \mathbf{FM}|\mathbf{dX}| \implies |\mathbf{dx}|^2 = \mathbf{M} \cdot (\mathbf{CM}) |\mathbf{dX}|^2. \quad (18)$$

So that the *stretch* between line elements \mathbf{dx} and \mathbf{dX} is

$$\lambda(\mathbf{M}) = \frac{|\mathbf{dx}|}{|\mathbf{dX}|} = |\mathbf{FM}| \equiv (\mathbf{M} \cdot (\mathbf{CM}))^{\frac{1}{2}}. \quad (19)$$

Similarly, for line elements \mathbf{dX} and \mathbf{dX}' with unit tangent vectors \mathbf{M} and \mathbf{M}' at points \mathbf{X} and \mathbf{X}' in the reference configuration; these fibers correspond to \mathbf{dx} and \mathbf{dx}' with unit vectors \mathbf{m} and \mathbf{m}' at points \mathbf{x} and \mathbf{x}' in the current configuration. Let β denote the angle between the directions \mathbf{M} and \mathbf{M}' and let α be the angle between directions \mathbf{m} and \mathbf{m}' ; then

$$\mathbf{dx} = \mathbf{FdX}, \quad \mathbf{dx}' = \mathbf{FdX}', \quad \beta = \cos^{-1}(\mathbf{M} \cdot \mathbf{M}'), \quad (20a)$$

$$\text{and } \alpha = \cos^{-1}(\mathbf{m} \cdot \mathbf{m}') = \cos^{-1}(\mathbf{M} \cdot (\mathbf{CM}')) / \lambda(\mathbf{M}) \cdot \lambda(\mathbf{M}'). \quad (20b)$$

In the plane of shear of \mathbf{M} and \mathbf{M}' , the *angle of shear* between the material line elements is the reduction in angles

$$\phi = \beta - \alpha. \quad (21)$$

Notice that both (17), and (19) are characterized by the stretch $\lambda = r/R$ and the radius in the current configuration (c.f. [1]). Therefore, we take the kinematic quantities that characterize the IAB deformation as

$$\mathbf{r} = \begin{bmatrix} \lambda \\ \phi \end{bmatrix} = \begin{bmatrix} r/R \\ \beta - \alpha \end{bmatrix} \quad (22)$$

i.e. \mathbf{r} is a function of material stretch, and the angle of shear between material line elements.

3.4 Stress Response from Strain Energy

We are concerned with the magnitudes of the differential stress on the IAB shells from a mechanical point of view and *our approach is based on a continuum mechanics viewpoint which is independent of finite element methods*. Since the IAB deforms at ambient temperature, we take thermodynamic properties such as temperature and entropy to have negligible contribution. The IAB material stress response, \mathbf{G} , at any point on the IAB's boundary at time t determines the Cauchy stress, $\boldsymbol{\sigma}$, as well as the history of the motion up to and at the time t [40]. The *constitutive equation* that relates the stress to an arbitrary motion will be determined using [41]'s *determinism for the stress principle*. The constitutive relation for the nominal stress deformation for an elastic IAB material is given by

$$\boldsymbol{\sigma} = \begin{pmatrix} \sigma_{rr} & \sigma_{r\theta} & \sigma_{r\phi} \\ \sigma_{\theta r} & \sigma_{\theta\theta} & \sigma_{\theta\phi} \\ \sigma_{\phi r} & \sigma_{\phi\theta} & \sigma_{\phi\phi} \end{pmatrix} = \mathbf{G}(\mathbf{F}) + q \mathbf{F} \frac{\partial \boldsymbol{\Lambda}}{\partial \mathbf{F}}(\mathbf{F}), \quad (23)$$

¹ \mathbf{dx} and \mathbf{dX} are respectively the material line elements at the points \mathbf{x} and \mathbf{X} in their respective configurations *i.e.* \mathcal{B}_0 , \mathcal{B} .

where \mathbf{G} is a functional with respect to the configuration χ , q acts as a Lagrange multiplier, and $\boldsymbol{\Lambda}$ denotes the internal

(incompressibility) constraints of the IAB system. For an incompressible material, the indeterminate Lagrange multiplier becomes the hydrostatic pressure *i.e.* $q = -p$ [42]. The incompressibility of the IAB material properties imply that $\Lambda \equiv \det \mathbf{F} - 1$. We can verify that

$$\boldsymbol{\sigma} = \mathbf{G}(\mathbf{F}) - p\mathbf{I} \quad (24)$$

since $\det(\mathbf{F}) = 1$. In terms of the stored strain energy, we find that

$$\boldsymbol{\sigma} = \frac{\partial \Psi}{\partial \mathbf{F}} \mathbf{F}^T - p\mathbf{I} \quad (25)$$

where \mathbf{I} is the identity tensor and p represents an arbitrary hydrostatic pressure. It follows that the constitutive law that governs the Cauchy stress tensor is

$$\begin{aligned} \boldsymbol{\sigma} &= \frac{\partial \Psi_{\text{iso}}}{\partial \mathbf{I}_1} \frac{\partial \mathbf{I}_1}{\partial \mathbf{F}} \mathbf{F}^T + \frac{\partial \Psi_{\text{iso}}}{\partial \mathbf{I}_2} \frac{\partial \mathbf{I}_2}{\partial \mathbf{F}} \mathbf{F}^T + \frac{\partial \Psi_{\text{mesh}}}{\partial \mathbf{I}_4} \frac{\partial \mathbf{I}_4}{\partial \mathbf{F}} \mathbf{F}^T - p\mathbf{I} \\ &= \frac{1}{2} C_1 \frac{\partial \text{tr}(\mathbf{FF}^T)}{\partial \mathbf{F}} \mathbf{F}^T + \frac{1}{2} C_2 \frac{\partial \text{tr}([\mathbf{F}^T \mathbf{F}]^{-1})}{\partial \mathbf{F}} \mathbf{F}^T \\ &\quad + C_4(I_4 - 1) \left[\frac{\partial (\mathbf{M} \cdot \mathbf{CM})}{\partial \mathbf{F}} + \frac{\partial (\mathbf{M}' \cdot \mathbf{CM}')}{\partial \mathbf{F}} \right] - p\mathbf{I} \\ &= C_1 \mathbf{FF}^T - C_2 (\mathbf{F}^T \mathbf{F})^{-1} \\ &\quad + 2C_4(I_4 - 1) [(\mathbf{FM})(\mathbf{FM})^T + (\mathbf{FM}')(\mathbf{FM}')^T] - p\mathbf{I} \\ \boldsymbol{\sigma} &= C_1 \mathbf{B} - C_2 \mathbf{C}^{-1} + 2C_4(I_4 - 1) [\mathbf{m} \otimes \mathbf{m} + \mathbf{m}' \otimes \mathbf{m}'] - p\mathbf{I}. \end{aligned} \quad (26)$$

Expanding (26), we see that the shear stresses vanish and we are left with the normal stresses, given by

$$\begin{aligned} \sigma_{rr} &= -p + \frac{R^4}{r^4} C_1 - \frac{r^4}{R^4} C_2 - 2C_4 \frac{R^8}{r^8} \cos^2 \gamma \\ &\quad + 4C_4 \frac{R^{16}}{r^{16}} \cos^4 \gamma \end{aligned} \quad (27a)$$

$$\begin{aligned} \sigma_{\phi\phi} &= -p + \frac{(1+r)^2}{R^2} C_1 - \frac{R^2}{(1+r)^2} C_2 \\ &\quad - 2C_4(1+r)^4 \sin^2 \gamma \frac{(R^4 - 2(1+r)^4 \sin^2 \gamma)}{R^8} \end{aligned} \quad (27b)$$

$$\sigma_{\theta\theta} = -p + C_1 - C_2. \quad (27c)$$

A visualization of the component stresses of (27) on the outer shells of the IAB material is illustrated in Fig. 8.

3.5 Boundary-Value Problem of Traction

The dynamic problem is to find the stress at every point in the robot's body subjected to external forces under suitable boundary conditions. The soft elastic materials are normally positioned around the object so that body forces are applied only along the axial direction; the fixed direction of

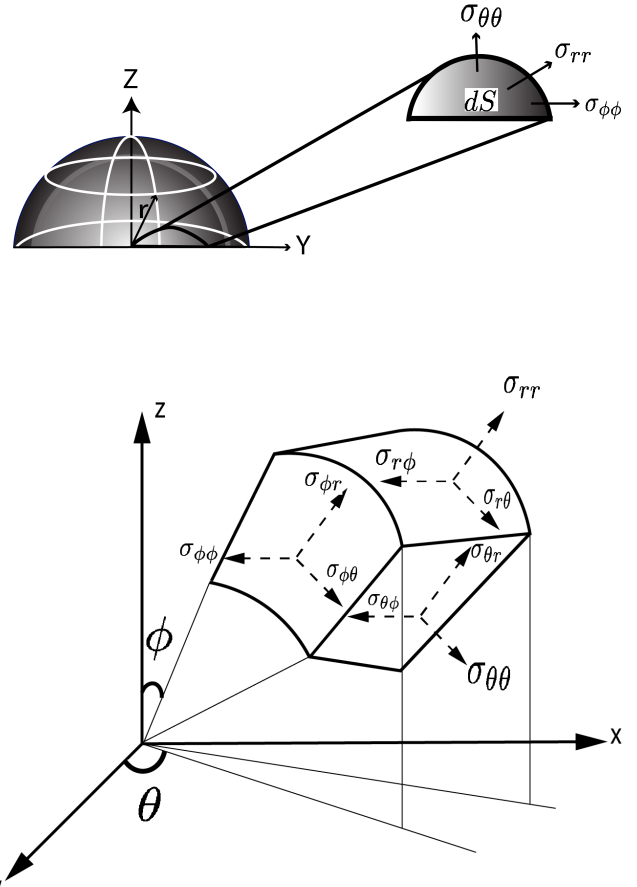


Fig. 8: Stress distribution on IAB's differential surface, dS .

axial loading implies that the deformation is a function of conservative forces only so that uniqueness of solution of stress field equations are preserved owing to Kirchoff's theorem [43, §7.4]. Furthermore, we assume that the applied pressure does not exceed a threshold that makes the rubber material yield to the point of buckling – thus, simplifying the solutions of the ensuing partial differential equations. The equilibrium equations for the physical component vectors of the body force, $\mathbf{b} = \{b_r, b_\phi, b_\theta\}$ are (see [1])

$$\begin{aligned} -b_r &= \frac{1}{r^2} \frac{\partial(r^2 \sigma_{rr})}{\partial r} + \frac{1}{r \sin \phi} \frac{\partial(\sin \phi \sigma_{r\phi})}{\partial \phi} + \\ &\quad \frac{1}{r \sin \phi} \frac{\partial}{\partial \theta} \sigma_{r\theta} - \frac{1}{r} (\sigma_{\theta\theta} + \sigma_{\phi\phi}) \end{aligned} \quad (28a)$$

$$\begin{aligned} -b_\phi &= \frac{1}{r^3} \frac{\partial(r^3 \sigma_{r\phi})}{\partial r} + \frac{1}{r \sin \phi} \frac{\partial(\sin \phi \sigma_{\phi\phi})}{\partial \phi} + \frac{1}{r \sin \phi} \frac{\partial(\sigma_{\theta\phi})}{\partial \theta} \\ &\quad - \frac{\cot \phi}{r} (\sigma_{\theta\theta}) \end{aligned} \quad (28b)$$

$$\begin{aligned} -b_\theta &= \frac{1}{r^3} \frac{\partial(r^3 \sigma_{\theta\theta})}{\partial r} + \frac{1}{r \sin^2 \phi} \frac{\partial(\sin^2 \phi \sigma_{\phi\phi})}{\partial \phi} + \frac{1}{r \sin \phi} \frac{\partial}{\partial \theta} \sigma_{\theta\theta}. \end{aligned} \quad (28c)$$

Owing to the CCOARSE symmetry of the elastic IAB materials, all shearing stresses *i.e.* $\sigma_{r\theta}, \sigma_{\phi\theta}, \sigma_{r\phi}$ etc., vanish. We prescribe the following boundary conditions for the radial

normal stress

$$\sigma_{rr}|_{r=r_o} = -P_{\text{atm}}, \quad \sigma_{rr}|_{r=r_i} = -P_{\text{atm}} - P \quad (29)$$

where P_{atm} is the atmospheric pressure and $P > 0$ is the internal pressure exerted on the internal walls of the IAB above P_{atm} i.e., $P > P_{\text{atm}}$. Furthermore, we note that $\sigma_{\theta\theta} = 0$ owing to the CCOARSE circumferential constraint. Thus, (28) becomes

$$-b_r = \frac{1}{r^2} \frac{\partial(r^2 \sigma_{rr})}{\partial r} - \frac{\sigma_{\phi\phi}}{r} \quad (30a)$$

$$-b_\phi = \frac{1}{r \sin \phi} \frac{\partial}{\partial \phi} (\sin \phi \sigma_{\phi\phi}), \quad -b_\theta = 0. \quad (30b)$$

Expanding (30a) and substituting (29), we can verify that

Internal Pressure and Radial Body Force

$$P = \int_{r_i}^{r_o} \frac{1}{r} (rb_r + \sigma_{\phi\phi} - 2\sigma_{rr}) dr \quad (31)$$

where r_i and b_r are known. Under the incompressibility properties of the IAB material we have,

$$r^3 = R^3 + r_i^3 - R_i^3, \text{ and } r_o^3 = R_o^3 + r_i^3 - R_i^3. \quad (32)$$

Equations (31) and (32) completely determine the inverse kinematics (SOFT IK) of the IAB material: for a required IAB deformation, it determines the internal pressurization or normal Cauchy stress required.

4 Analysis of Contact Kinematics

The interactions among the manipulators and head are considered as a classical case of elastic bodies in contact. Using the soft finger contact primitive [44], the IAB forces and torques are modeled within a “cone of forces” about the direction of the surface normal from the object (in this case the head) (see Fig. 9). The trajectory of the head under the influence of motion of an IAB is influenced by the position vector \mathbf{r} of (22). When the IAB deforms, body forces in its current configuration and the *traction* over its boundary $\partial\mathcal{B}$ impact motion on the head. Constrained by the frictional coefficient, we define the soft contact force inside the friction cone as

$$\tilde{\mathbf{F}}_{ci} = \begin{pmatrix} \mathbf{I} & 0 \\ 0 & n_{ci} \end{pmatrix} \begin{pmatrix} f_{ci} \\ \tau_{ci} \end{pmatrix}, \quad (33)$$

where $f_{ci} \in \mathbb{R}^3$ denotes the amount of force exerted by the IAB along the direction of contact, $\tau_{ci} \in \mathbb{R}$ is the moment of the contact force, and n_{ci} is the *normal* or *Gauss map*² for

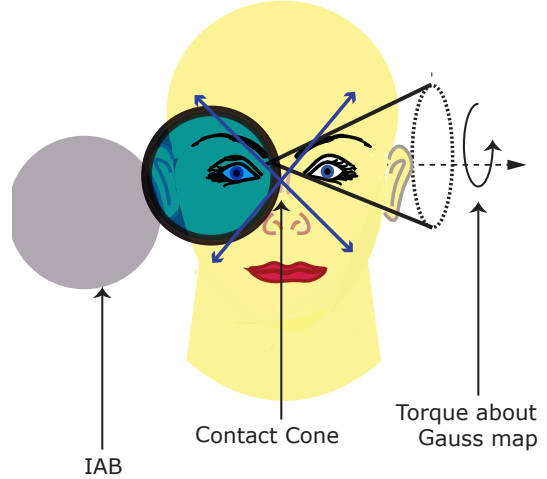


Fig. 9: Soft Contact Illustration

a manifold $S \subset \mathbb{R}^3$ of a head surface. For contact models with friction, we require that all contact forces lie within the friction cone, determined by the frictional coefficient. The set of forces within or on the boundary of the friction cone is

$$FC = \{f_c \in \mathbb{R}^n : \|f_{cij}^t\| \leq \mu_{ij} \|f_{ci}^n\|, \\ i = 1, \dots, k, j = 1, \dots, m_i\} \quad (34)$$

where f_{cij}^t is the tangent component of the j^{th} element of the contact force, f_{ci}^n is i^{th} contact's normal force, and μ_{ij} is f_{cij} 's coefficient of friction.

4.1 Contact/Traction Forces and Stress Equivalence

Here, we relate the microscopic contact stress of the previous section with the macroscopic descriptions of the contact friction to enable us treat different material combinations for the manipulator and head. We assume that the stress vector $\boldsymbol{\sigma}$ at a point on the IAB surface is uniform and continuous throughout the IAB boundary so that it linearly depends on the normal map (this follows from Cauchy's theorem; readers may see the proof in [40, §3.3.1]). The correspondence between material line, $\{\mathbf{dx}, \mathbf{dX}\}$, elements in the reference and current configuration is

$$\mathbf{dx} = \mathbf{F} \mathbf{dX} \implies \mathbf{F}^{-T} \mathbf{dx} = \mathbf{dX}. \quad (35)$$

where \mathbf{F} is the deformation gradient.

Let $\mathbf{H} = \mathbf{F}^{-T}$ and \mathbf{da} represent an infinitesimal vector element on the material surface at a neighborhood of point \mathbf{X} in \mathcal{B} such that $\mathbf{da} = \mathbf{n} da$, where \mathbf{n} is the unit outward normal

²A normal map for a manifold S is a continuous map $g : S \rightarrow S^2 \subset \mathbb{R}^3$ such that for every $s \in S$, $g(s)$ is orthogonal to S at s [45].

to the IAB surface. On the bounding surface of the IAB the exerted force on a surface area \mathbf{da} in global form is

$$\mathbf{f}_c = \int_{\partial\mathcal{B}} \boldsymbol{\sigma} \mathbf{n} d\mathbf{a}. \quad (36)$$

At the region of contact, we have the i 'th contact force within the friction cone as

$$\begin{aligned} f_{ci} &= (\sigma_{rr} + \sigma_{\phi\phi}) n_{ci} da_i \\ f_{ci} &= \left[-2p + \frac{r^4 + 2r^5 + r^6 + R^6}{r^2 R^2} \left(\frac{C_1}{r^2} - \frac{r^2}{(1+r)^2 R^2} C_2 \right) \right. \\ &\quad + 2 \cos^2 \gamma \frac{R^8}{r^8} \left(\cos^2 \gamma \frac{R^8}{r^8} - 1 \right) C_4 \\ &\quad \left. - \frac{(1+r)^4}{R^8} \sin^4 \gamma \cos(2\gamma) \right. \\ &\quad \left. (-1 - 4r - 6r^2 - 4r^3 - r^4 + 2R^4 + (1+r)^4) C_4 \right] n_{ci} da_i. \end{aligned} \quad (37)$$

with the outward normal map n_{ci} from (33). The torque is the moment of the contact force on the i 'th IAB, given as

$$\tau_{ci} = f_{ci} \times r_{ci} \quad (38)$$

where $r_{ci} \in \mathbb{R}^3$ is the unit vector between the head reference point and the contact. Therefore, we have (33) as

Friction Cones' Contact Force

$$\tilde{F}_{ci} = \begin{bmatrix} \mathbf{I} & 0 \\ 0 & n_{ci} \end{bmatrix} \begin{bmatrix} (\sigma_{rr} + \sigma_{\phi\phi}) n_{ci} da_i \\ (\sigma_{rr} + \sigma_{\phi\phi}) n_{ci} da_i \times r_{ci} \end{bmatrix}. \quad (39)$$

4.2 Contact Coordinates and Head Velocity

The head will make contact with the IAB at multiple points on its surface, so we describe the kinematics of these contact points using an atlas³ of contact coordinate charts. In this sentiment, let C_{r_1} and C_{r_h} respectively represent a fixed reference frame with respect to the IAB and head, H (see Fig. 10). Furthermore, let $S_1 \subset \mathbb{R}^3$ and $S_h \subset \mathbb{R}^3$ denote the respective *orientable manifold*⁴ embeddings of the IAB and head surfaces with respect to frames C_{r_1} and C_{r_h} . We shall let S_1 and S_h belong to the atlases $\{S_{1,i}\}_{i=1}^{n_1}$, $\{S_{h,i}\}_{i=1}^{n_h}$ respectively. Suppose (f_i, U_i) and (f_h, U_h) are *coordinate systems* for the IAB and the head respectively, where f_i is an invertible map, $f_i(u_i, v_i) : U \rightarrow S_i \subset \mathbb{R}^3$

$$f_i(u_i, v_i) : \{U \rightarrow S_i \subset \mathbb{R}^3 | i = 1, h\},$$

³An atlas $\tilde{\mathcal{S}}$ is a set of surfaces where each surface $S \in \tilde{\mathcal{S}}$ has an invertible map $f(\mathbf{u})$ from an open subset U of \mathbb{R}^2 to a surface $S \subset \mathbb{R}^3$ such that the partial derivatives $\frac{\partial f}{\partial u}(\mathbf{u})$, $\frac{\partial f}{\partial v}(\mathbf{v})$ are linearly independent for all $\mathbf{u} = (u, v) \in U$.

⁴An orientable manifold is a manifold S for which the Gauss map exists.

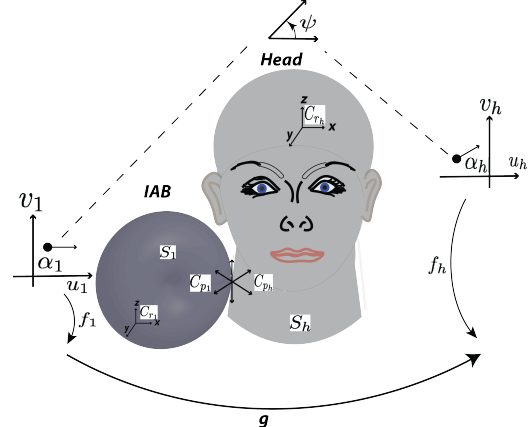


Fig. 10: Sliding and rolling contact illustration of a single IAB and the Head. [Image best visualized in colored ink].

from an open subset U of \mathbb{R}^2 to a *coordinate patch* $S_i \subset \mathbb{R}^3$ such that the partial derivatives $\frac{\partial f_i}{\partial u_i}$ and $\frac{\partial f_i}{\partial v_i}$ are linearly independent. Let $p_1(t) \in S_1$ and $p_h(t) \in S_h$ represent the positions of the contact points with respect to frames C_{r_1} and C_{r_h} respectively at time t . In general, the contact points $p_1(t)$ and $p_h(t)$ will not remain in the coordinate systems S_1 and S_h for all time. Thus, we choose an interval I where $p_1(t) \in S_{1,i}$ and $p_h(t) \in S_{h,j}$ for all $t \in I$ and some i and j . As seen in Fig. 10, C_{p_1} and C_{p_h} denote the contact frames that coincide with the *normalized Gauss frames* at p_1 and p_h for all $t \in I$, and α_1 , α_h are local coordinate frames that describe the IAB motion with respect to the head such that

$$\alpha_1 = (u_1, v_1) \in U_1, \text{ and } \alpha_h = (u_h, v_h) \in U_h. \quad (40)$$

Let the angle between the tangent planes of α_1 , and α_h be ψ . The transformation matrix $g \in \Omega \subset SE(3)$ encodes the relative orientation and position of the IAB with respect to the head where Ω is the set of all relative positions and orientations in the atlases $\{S_{1,i}\}_{i=1}^{n_1}$, $\{S_{h,i}\}_{i=1}^{n_h}$ for which the IAB and head remain in contact. We let the *contact coordinates* be described by $\eta = (\alpha_1, \alpha_h, \psi)$. The head's motion is governed by traction forces arising from the friction tangential to the IAB surface and the pressure normal to the IAB surface. Thus, at the points of contact, if $R \in SO(3)$ is the rotatory component of g , η must satisfy

$$g \circ f_1(\alpha_1) = f_h(\alpha_h) \quad (41a)$$

$$R n_1(\alpha_1) = -n_h(\alpha_h) \quad (41b)$$

since the contact locations must coincide for the IAB and the head, and the tangent planes must coincide so that the outward normal maps $n_1 : S_1 \rightarrow S^2 \subset \mathbb{R}^3$ and $n_h : S_h \rightarrow S^2 \subset \mathbb{R}^3$ agree. Furthermore, the orientation of the tangent planes of α_1 and α_h is the unique angle $\psi \in [0, 2\pi)$ between the

x -axes of C_{p_1} and C_{p_h} such that

$$R \frac{\partial f_1}{\partial \alpha_1} M_1^{-1} R_\Psi = \frac{\partial f_h}{\partial \alpha_h} M_h^{-1} \quad (42)$$

where M_i is a 2×2 square root of the Riemannian metric tensor [46] that normalizes the columns of $\frac{\partial f}{\partial \alpha}$, i.e.

$$M_i = \begin{bmatrix} \|\frac{\partial f_i}{\partial u_i}\| & 0 \\ 0 & \|\frac{\partial f_i}{\partial v_i}\| \end{bmatrix} \quad (43)$$

and R_Ψ is chosen such that a rotation of C_{p_1} about its z -axis through $-\psi$ radians aligns the x -axes of the local coordinate system α_1 to that of the head's local coordinate system α_h i.e.

$$R_\Psi = \begin{bmatrix} \cos \psi & -\sin \psi \\ -\sin \psi & -\cos \psi \end{bmatrix} \quad (44)$$

with the special property that $R_\Psi = R_\Psi^T = R_\Psi^{-1}$. We define the normalized Gauss frame at a point u on the surface U of the orthogonal coordinate system (f, U) as,

$$[x_u \ y_u \ z_u] = \left[\frac{\partial f}{\partial u} / \left\| \frac{\partial f}{\partial u} \right\| \ \frac{\partial f}{\partial v} / \left\| \frac{\partial f}{\partial v} \right\| \ n_u(f(u)) \right] \quad (45)$$

where x_u , y_u , and z_u are functions mapping $U \subset \mathbb{R}^2 \rightarrow \mathbb{R}^3$ and n_u is the continuous Gauss map $n_u : S \rightarrow S^2 \subset \mathbb{R}^3$. The motion of the contacts $\dot{\eta}$ as a function of components of the twist vector $\dot{\xi} = (v, w)^T$ is given in (46) as the respective *first*, *second*, and *third equations of contact*. We can verify that (see proof in Appendix B of [2])

$$\dot{\alpha}_h = M_h^{-1} (\mathcal{K}_h + \tilde{\mathcal{K}}_l)^{-1} (\omega_t - \tilde{\mathcal{K}}_l v_t) \quad (46a)$$

$$\dot{\alpha}_1 = M_1^{-1} R_\Psi (\mathcal{K}_h + \tilde{\mathcal{K}}_l)^{-1} (\omega_t - \mathcal{K}_h v_t) \quad (46b)$$

$$\dot{\psi} = \omega_n + T_h M_h \dot{\alpha}_h + T_1 M_1 \dot{\alpha}_1 \quad (46c)$$

where

$$\begin{aligned} T_h &= y_h^T \frac{\partial x_h}{\partial \alpha_h} M_h^{-1}, \quad T_1 = y_1^T \frac{\partial x_1}{\partial \alpha_1} M_1^{-1}, \\ \mathcal{K}_h &= [x_h^T, y_h^T]^T \frac{\partial n_h^T}{\partial \alpha_h} M_h^{-1}, \quad \omega_n = z_h^T \omega \\ \mathcal{K}_l &= R_\Psi [x_1^T, y_1^T]^T \frac{\partial n_1^T}{\partial \alpha_1} M_1^{-1} R_\Psi, \\ \omega_t &= [x_h^T, y_h^T]^T [n_h \times \omega]^T, \\ \text{and } v_t &= [x_h^T, y_h^T]^T [(-f_h \times \omega + v)]^T. \end{aligned} \quad (47)$$

Note that ω_t is the rolling velocity of the head projected onto the tangent plane of the contact and v_t is the sliding velocity;

ω_n is the relative rotational velocity projected to the contact's surface normal, and $\tilde{\mathcal{K}}_l = R_\Psi \mathcal{K}_l R_\Psi$ is the curvature of the IAB with respect to the contact frame that coincides with the normalized Gauss frame at $p_1(t)$. The matrix $(\mathcal{K}_h + \tilde{\mathcal{K}}_l)^{-1}$ is the so-called *relative curvature* originally coined by [45]. Simplifying (47), we find that

$$\begin{aligned} x_h &= \frac{\partial f}{\partial u_h} / \left\| \frac{\partial f}{\partial u_h} \right\|, \quad y_h = \frac{\partial f}{\partial v_h} / \left\| \frac{\partial f}{\partial v_h} \right\|, \quad z_h = n_u(f(u)) \\ T_h &= y_h \left[\frac{\partial x_h^T}{\partial u_h} / \left\| \frac{\partial f}{\partial u_h} \right\|, \frac{\partial x_h^T}{\partial v_h} / \left\| \frac{\partial f}{\partial v_h} \right\| \right], \\ T_1 &= y_1 \left[\frac{\partial x_1^T}{\partial u_1} / \left\| \frac{\partial f}{\partial u_1} \right\|, \frac{\partial x_1^T}{\partial v_1} / \left\| \frac{\partial f}{\partial v_1} \right\| \right], \\ \mathcal{K}_h &= [x_h^T, y_h^T]^T \left[\frac{\partial n_h^T}{\partial u_h} / \left\| \frac{\partial f}{\partial u_h} \right\|, \frac{\partial n_h^T}{\partial v_h} / \left\| \frac{\partial f}{\partial v_h} \right\| \right], \\ \mathcal{K}_l &= [x_1^T, y_1^T]^T \left[\frac{\partial n_1^T}{\partial u_1} / \left\| \frac{\partial f}{\partial u_1} \right\|, \frac{\partial n_1^T}{\partial v_1} / \left\| \frac{\partial f}{\partial v_1} \right\| \right]. \end{aligned} \quad (48)$$

We see that for the contact interaction between an IAB and the head, for a $U \subset \mathbb{R}^2$ we must choose an appropriate $f_i : U_i \rightarrow S_i \subset \mathbb{R}^3$ in order to characterize the setup.

5 System's Newton-Euler Equations

From Truesdell's *determinism for the stress principle* [41], the Cauchy stress σ at any point in a material at time t for any motion up to time t determines the stress response of the material for any arbitrary motion history up to and including time t . We will derive the dynamics of the IAB system in the *strain field of the deformation*. The potential and kinetic energy of the system are considered to be derived from the constitutive strain field relations that characterize the deformation. We now use Lagrangian deformation analysis to derive the dynamic equations of the continuum multi-IAB system.

For a soft continuum body, there is an enormous amount of particle orientations during deformation; the number of particle states that is physically measurable with sensors instantaneously in a given configuration is overwhelming. However, we can leverage the constitutive law which describes the macroscopic IAB material behavior with respect to a reference frame, S , at a time, t by completely characterizing it by ten dependent variables viz., three components of the position vector, six component stress tensor variables (the shear and normal stress components), and

5.1 Euler-Lagrange Equations

Following § 3.3, we are only interested in the final position and orientation of the IAB as a whole rather than the system of particles that characterize a deformation at every time t . When the head exerts a reactive wrench on an IAB, it is natural to expect a dent. The shear angle in (22) should capture the amount of angular deformation. For a kinetic energy T and a potential energy V , the *Lagrangian*, L , of the system in generalized coordinates is the difference between the kinetic and potential energy, i.e.

$$L(\mathbf{r}, \dot{\mathbf{r}}) = T(\mathbf{r}, \dot{\mathbf{r}}) - V(\mathbf{r}). \quad (49)$$

The equations of motion for a pneumatic IAB system is of the form

$$\frac{d}{dt} \frac{\partial L}{\partial \dot{\mathbf{r}}_i} - \frac{\partial L}{\partial \mathbf{r}_i} = \boldsymbol{\tau}_i, \quad i = 1, \dots, m \quad (50)$$

where $\boldsymbol{\tau}_i$ is the torque acting on the i^{th} generalized coordinate. Written in matrix form equation, we can write the Euler-Lagrange equation of (50) as

$$\frac{d}{dt} \frac{\partial L}{\partial \dot{\mathbf{r}}} - \frac{\partial L}{\partial \mathbf{r}} = \boldsymbol{\tau}. \quad (51)$$

It now remains to derive the kinetic and potential energies for the IAB material. Let the velocity of an IAB material particle \mathbf{x} in the current configuration at time t be $\mathbf{v}(\mathbf{r}, t)$, then the Eulerian velocity gradient tensor can be defined as

$$\boldsymbol{\Gamma} = \text{grad } \mathbf{v}(\mathbf{r}, t). \quad (52)$$

Cauchy's first law of motion [1, eq. 19] will allow us to derive the balance of mechanical energy of the system. Multiplying throughout by \mathbf{v} , we find that

$$\begin{aligned} \text{div} (\boldsymbol{\sigma}^T \cdot \mathbf{v}) + \rho \mathbf{b} \cdot \mathbf{v} &= \rho \mathbf{v} \cdot \dot{\mathbf{v}} \\ \text{or div} (\boldsymbol{\sigma}^T \mathbf{v}) - \mathbf{tr}(\boldsymbol{\sigma} \boldsymbol{\Gamma}) + \rho \mathbf{b} \cdot \mathbf{v} &= \rho \mathbf{v} \cdot \dot{\mathbf{v}}. \end{aligned} \quad (53)$$

where ρ is the IAB's mass density. Following mass conservation, we integrate over volume \mathcal{B} and employ the divergence theorem, so that the above relation yields the *balance of mechanical energy*

$$\begin{aligned} \int_{\mathcal{B}} \rho \mathbf{b} \cdot \mathbf{v} dv + \int_{\partial \mathcal{B}} f_p \cdot \mathbf{v} da &= \frac{d}{dt} \int_{\mathcal{B}} \frac{1}{2} \rho \mathbf{v} \cdot \mathbf{v} dv \\ &\quad + \int_{\mathcal{B}} \mathbf{tr}(\boldsymbol{\sigma} \boldsymbol{\Gamma}) dv \end{aligned} \quad (54)$$

where f_p is the IAB body force density, and the left hand side of the foregoing is the so-called *rate of working of the applied forces*. The symmetry of the stress tensor $\boldsymbol{\sigma}$ implies that $\mathbf{tr}(\boldsymbol{\sigma} \boldsymbol{\Gamma}) = \mathbf{tr}(\boldsymbol{\sigma} \boldsymbol{\Sigma})$ where $\boldsymbol{\Sigma}$ is given in terms of the Eulerian-strain rate tensor, $\boldsymbol{\Gamma}$ *i.e.*,

$$\boldsymbol{\Sigma} = \frac{1}{2} (\boldsymbol{\Gamma} + \boldsymbol{\Gamma}^T) \quad (55)$$

so that the kinetic energy density and stress power are

$$T(\mathbf{r}, \dot{\mathbf{r}}) = \frac{1}{2} \rho \mathbf{v} \cdot \mathbf{v}, \quad V(\mathbf{r}) = \mathbf{tr}(\boldsymbol{\sigma} \boldsymbol{\Sigma}). \quad (56)$$

5.2 Case I: Euler-Lagrange Equation for Cauchy-Elastic IAB Material

The stress-strain relation for the IAB we have presented are only related through the deformation tensor, implying that the material is Cauchy elastic. For Cauchy elastic materials, the stress power term is not conserved during deformation making integration over the material body \mathcal{B} physically unrealistic [40]. For such materials, we may set the stored strain energy V to an arbitrary constant (*e.g.* $V(I) = 0$). We can derive the torque dynamics of an IAB actuator as (see proof in Appendix B)

$$\boldsymbol{\tau} = \underbrace{\begin{bmatrix} \rho/R^2 & 0 \\ 0 & \rho \end{bmatrix}}_{M_{iab}} \ddot{\mathbf{r}} + \underbrace{\begin{bmatrix} \rho \dot{r}/R^3 & 0 \\ 0 & 0 \end{bmatrix}}_{C_{iab}} \dot{\mathbf{r}}. \quad (57)$$

Rewriting equation (57) in terms of the torque for each soft robot, we have the dynamics for IAB j as

$$M_{iab_j}(\mathbf{r}_j) \ddot{\mathbf{r}}_j + C_{iab_j}(\mathbf{r}_j, \dot{\mathbf{r}}_j) \dot{\mathbf{r}}_j = \boldsymbol{\tau}_j \quad (58)$$

where M_{iab_j} and C_{iab_j} contain the respective inertia and Coriolis forces for actuator j . Since the IAB material is incompressible, the mass density is uniform throughout the body of the material. In general, we write equation (58) as

$$M_{iab}(\tilde{\mathbf{r}}) \ddot{\tilde{\mathbf{r}}} + C_{iab}(\tilde{\mathbf{r}}, \dot{\tilde{\mathbf{r}}}) \dot{\tilde{\mathbf{r}}} = \tilde{\boldsymbol{\tau}} \quad (59)$$

where $\tilde{\mathbf{r}} \in \mathbb{R}^{n_1} \times \mathbb{R}^{n_2} \times \dots \times \mathbb{R}^{n_8}$ gives the generalized coordinates for all the IABs and $\tilde{\boldsymbol{\tau}}$ are the vectorized torques of the individual robots.

5.3 Case II: Euler-Lagrange Equation for Green Elastic IAB Material

For completeness, we treat the case where the IAB material body is *hyperelastic* (*i.e.*, *Green elastic*)⁵, the eulerian form of the stress power expression is

$$V(\mathbf{r}) = \mathbf{tr}(\boldsymbol{\sigma} \boldsymbol{\Sigma}). \quad (60)$$

We are mostly interested in the mechanical energy in the current configuration, however, it is worthwhile to note that the equivalent relation in the Lagrangean form is

$$\begin{aligned} \int_{\mathcal{B}_o} \rho_o \mathbf{b}_o \dot{\mathbf{X}} dV + \int_{\partial \mathcal{B}_o} (\boldsymbol{\sigma}^T \mathbf{N}) \dot{\mathbf{X}} dA &= \\ \frac{d}{dt} \int_{\mathcal{B}_o} \frac{1}{2} \rho_o \dot{\mathbf{X}} \cdot \dot{\mathbf{X}} dV + \int_{\mathcal{B}_o} \mathbf{tr}(\boldsymbol{\sigma} \dot{\mathbf{F}}) dV, \end{aligned} \quad (61)$$

It follows that,

$$V(\mathbf{r}) = \mathbf{tr}(\boldsymbol{\sigma} \dot{\mathbf{F}}) \quad (62)$$

⁵An hyperelastic material is one where the strain-energy function exists.

for a Green elastic material. Similar to the arguments in § 5.2, we find the torque as (see derivation in Appendix B)

Green-Elastic IAB Material Torque

$$\boldsymbol{\tau} = \frac{\rho \ddot{r}}{R^2} + \rho \ddot{\alpha} + \frac{\rho \dot{r}^2}{R^3} + 4C_1 \left(\frac{2R^3}{r^5} + \frac{r}{R^3} \right) + 4C_2 \left(\frac{2r^3}{R^5} + \frac{R}{r^3} \right). \quad (63)$$

6 Mechanism Statics and Kinetics

6.1 End Effector Forces

From the derived relationship between the head contact coordinates and the relative motion (v_t, ω_t) of the IAB *i.e.* equation (46), we can associate a Jacobian that maps IAB velocities to head position and orientation. A fundamental assumption in our formulation is that the IABs make contact with the head throughout manipulation, and the manipulation is stable and prehensile. A forward kinematic map from the configuration of the i^{th} IAB, χ_{iab_i} maps from respective IAB configurations to head position and orientation *i.e.* $K_{iab_i} : \chi_{iab_i} \rightarrow SE(3)$. The velocity of the head with respect to a fixed base frame in terms of IAB velocities can be written in terms of the forward kinematics Jacobian:

$$\begin{pmatrix} v_{iab_i} \\ \omega_{iab_i} \end{pmatrix} = \frac{\partial K_{iab_i}}{\partial \mathbf{r}_i} \frac{d\mathbf{r}}{dt} K_{iab_i}^{-1} = \mathbf{J}_i(\mathbf{r}_i) \dot{\mathbf{r}}_i \quad (64)$$

where \mathbf{r}_i is the spatial position of IAB i , and $(v_{iab_i}^T, \omega_{iab_i}^T) \in \mathbb{R}^6$ represents the linear and angular velocity of the i^{th} IAB about its screw basis. In essence, $\mathbf{r}_i \in \mathbb{R}^3$ with its rows of mapped to scalars by an appropriate choice of norm. The contact between the head and the IABs is mapped by the Jacobian

$$\mathbf{J}_{c_i}(\xi_h, \xi_{iab_i}) = \begin{bmatrix} \mathbf{I} & \hat{\mathbf{w}}(r_{c_i}) \\ \mathbf{0} & \mathbf{I} \end{bmatrix} J_{r_i}, \quad (65)$$

where $\mathbf{J}_{c_i} : \dot{\xi}_{r_i} \rightarrow [v_{c_i}^T, w_{c_i}^T]^T$, $r_{c_i} \in \mathbb{R}^3$ is a vector between the head reference point (e.g. the center of mass) and the contact with the i^{th} IAB, ξ_h is the position and relative orientation of the head, ξ_{iab_i} is the position and relative orientation of the i^{th} soft robot in world coordinates, $\hat{\mathbf{w}}(r_{c_i})$ is an anti-symmetric matrix for the vector r_{c_i} , and $\xi_r = (\xi_{r_1}, \xi_{r_2}, \dots, \xi_{r_8})$ are the positions and orientations for each of the 8 IABs. The manipulation map, G_i is made up of matrices of the form

$$G_i(\xi_h, \xi_r) = \begin{bmatrix} \mathbf{I} & \mathbf{0} \\ \hat{\mathbf{w}}(r_{c_i}) & \mathbf{I} \end{bmatrix} B_i(\xi_h, \xi_r), \quad (66)$$

where $B_i(\xi_h, \xi_r)$ is the selection map as defined in [48] for the desired manipulation. The net force on the head is a sum

of the individual forces arising from each IAB. Owing to the linearity of each individual IAB's contact force, the resultant head force can be stitched together to form G , *i.e.*

$$\tilde{F}_h = [G_1, \dots, G_8] \begin{pmatrix} \tilde{F}_{c_1} \\ \vdots \\ \tilde{F}_{c_8} \end{pmatrix} = G \tilde{F}_c, \quad (67)$$

where $F_h \in \mathbb{R}^6$ and $F_c \in \mathbb{R}^{m_1} \times \mathbb{R}^{m_2} \times \dots \times \mathbb{R}^{m_8}$. The *internal or null forces* is captured by the null space $\mathcal{N}(G)$ of the manipulation map G ; these forces correspond to zero net force on the head of the patient. Each \tilde{F}_{c_i} in (67) is of the form (39).

6.2 End-effector Velocities

We define the velocity constraint dual of (66) as the constraint between the relative velocity of the head and that of the twist velocities of the contact point

$$\begin{pmatrix} \tilde{v}_{c_i} \\ \tilde{\omega}_{c_i} \end{pmatrix} = \begin{bmatrix} \mathbf{I} & \hat{\mathbf{w}}(r_{c_i}) \\ \mathbf{0} & \mathbf{I} \end{bmatrix} \begin{pmatrix} v_{c_h} \\ \omega_{c_h} \end{pmatrix}. \quad (68)$$

For a conjugate twist vector $(v_c^T, \omega_c^T)^T$ to the forces exerted by the IABs, f_c , we have the following

$$\begin{pmatrix} v_c \\ \omega_c \end{pmatrix} = G^T \begin{pmatrix} v_{c_h} \\ \omega_{c_h} \end{pmatrix}. \quad (69)$$

Given a *selection matrix* $B_i^T(\xi_h, \xi_{iab_i}) \in \mathbb{R}_i^m$ for a particular IAB, where m_i is the range of all the forces and moments for the chosen contact primitive (or union of contact primitives), the *manipulation map* for the i^{th} IAB can be written as,

$$G_i^T(\xi_h, \xi_{iab_i}) \xi_h = B_i^T(\xi_h, \xi_{iab_i}) \mathbf{J}_{c_i}(\xi_h, \mathbf{r}_{r_i}) \dot{\xi}_{iab_i} \quad (70)$$

where \mathbf{J}_{c_i} is the contact Jacobian for the i^{th} actuator, and ξ_h denotes the velocity of the head. For the 8 soft actuators, the manipulation constraint of the system can be written as

$$\begin{bmatrix} G_1^T \\ G_2^T \\ \vdots \\ G_8^T \end{bmatrix} \begin{pmatrix} v_h \\ w_h \end{pmatrix} = \text{diag} \begin{pmatrix} B_1^T \mathbf{J}_{c_1} \\ B_2^T \mathbf{J}_{c_2} \\ \vdots \\ B_8^T \mathbf{J}_{c_8} \end{pmatrix} \begin{pmatrix} \dot{\mathbf{r}}_{iab_1} \\ \dot{\mathbf{r}}_{iab_2} \\ \vdots \\ \dot{\mathbf{r}}_{iab_8} \end{pmatrix}. \quad (71)$$

7 Newton-Euler System of Equations

The dynamics of the head is a form of (59) but without the actuator torques. In local coordinates, it has the form

$$\mathbf{M}_h(\zeta) \ddot{\zeta} + \mathbf{C}_h(\zeta, \dot{\zeta}) \dot{\zeta} + \mathbf{N}_h(\zeta, \dot{\zeta}) = 0 \quad (72)$$

with ζ being a local parameterization of the position and orientation of the head in the Lie Group $SE(3)$, and \mathbf{N}_h being the gravitational and frictional forces exerted by/on the head. The head and the multi-DOF IAB system are connected via the manipulation constraint *i.e.*

$$G^T(\zeta, \mathbf{r})\dot{\zeta} = \mathbf{J}(\zeta, \mathbf{r})\dot{\mathbf{r}}. \quad (73)$$

Suppose that the velocity constraint produces a virtual displacement constraint in $\delta\zeta$ and $\delta\mathbf{r}$ such that for $q = (\zeta, \mathbf{r})$, we have

$$\delta\mathbf{r} = \mathbf{J}^{-1}(q)G^T(q)\delta\zeta$$

the Lagrange equations become

$$\left(\frac{d}{dt} \frac{\partial L}{\partial \dot{q}} - \frac{\partial L}{\partial q} - (\boldsymbol{\tau}, 0) \right) \delta q = 0 \quad (74a)$$

$$\begin{pmatrix} \frac{d}{dt} \frac{\partial L}{\partial \dot{\mathbf{r}}} - \frac{\partial L}{\partial \mathbf{r}} - \boldsymbol{\tau} \\ \frac{d}{dt} \frac{\partial L}{\partial \dot{\zeta}} - \frac{\partial L}{\partial \zeta} \end{pmatrix}^T \begin{pmatrix} \delta\mathbf{r} \\ \delta\zeta \end{pmatrix} = 0 \quad (74b)$$

$$\left(\frac{d}{dt} \frac{\partial L}{\partial \dot{\mathbf{r}}} - \frac{\partial L}{\partial \mathbf{r}} - \boldsymbol{\tau} \right) \delta\mathbf{r} + \left(\frac{d}{dt} \frac{\partial L}{\partial \dot{\zeta}} - \frac{\partial L}{\partial \zeta} \right) \delta\zeta = 0 \quad (74c)$$

$$G\mathbf{J}^{-T} \left(\frac{d}{dt} \frac{\partial L}{\partial \dot{\mathbf{r}}} - \frac{\partial L}{\partial \mathbf{r}} - \boldsymbol{\tau} \right) \delta\zeta + \left(\frac{d}{dt} \frac{\partial L}{\partial \dot{\zeta}} - \frac{\partial L}{\partial \zeta} \right) \delta\zeta = 0 \quad (74d)$$

wherefore,

$$\left(\frac{d}{dt} \frac{\partial L}{\partial \dot{\zeta}} - \frac{\partial L}{\partial \zeta} \right) \delta\zeta + G\mathbf{J}^{-T} \left(\frac{d}{dt} \frac{\partial L}{\partial \dot{\mathbf{r}}} - \frac{\partial L}{\partial \mathbf{r}} \right) = G\mathbf{J}^{-T} \boldsymbol{\tau} \quad (75)$$

given the arbitrariness of $\delta\zeta$. Equations (75) alongside (73) completely describe the system dynamics. Putting (58) into (75), we have

$$\left(\frac{d}{dt} \frac{\partial L}{\partial \dot{\zeta}} - \frac{\partial L}{\partial \zeta} \right) \delta\zeta = G\mathbf{J}^{-T} \left(1 - \frac{\rho}{2\|\mathbf{r}\|^2} \right) \boldsymbol{\tau}. \quad (76)$$

8 Conclusions

We have presented the constitutive model of these new class of soft actuators and we have presented the kinematic and dynamic equations that govern the behavior of the soft mechanism under mechanical loads. Future work will integrate the hardware for the tasks so described herein. Furthermore, in a follow-up paper (to be released shortly), we prescribe a trajectory optimization algorithm that uses the presented model on several manipulation and control tasks.

References

- [1] Ogunmolu, O., Liu, X., Gans, N., and Wiersma, R., 2020. “Mechanism and Constitutive Model of a Continuum Robot for Head and Neck Cancer Radiotherapy”. In IEEE International Conference on Robotics and Automation (ICRA), Paris, France.
- [2] Ogunmolu, O. P., 2019. “A Multi-DOF Soft Robot Mechanism for Patient Motion Correction and Beam Orientation Selection in Cancer Radiation Therapy”. PhD thesis, The University of Texas at Dallas; UT Southwestern Medical Center.
- [3] Bern, J. M., Chang, K.-H., and Coros, S., 2017. “Interactive design of animated plushies”. *ACM Transactions on Graphics (TOG)*, **36**(4), p. 80.
- [4] Bern, J. M., Kumagai, G., and Coros, S., 2017. “Fabrication, modeling, and control of plush robots”. In 2017 IEEE/RSJ International Conference on Intelligent Robots and Systems (IROS), IEEE, pp. 3739–3746.
- [5] Liu, T., Bouaziz, S., and Kavan, L., 2017. “Quasi-newton methods for real-time simulation of hyperelastic materials”. *ACM Transactions on Graphics (TOG)*, **36**(3), p. 23.
- [6] Bouaziz, S., Martin, S., Liu, T., Kavan, L., and Pauly, M., 2014. “Projective dynamics: fusing constraint projections for fast simulation”. *ACM Transactions on Graphics (TOG)*, **33**(4), p. 154.
- [7] Hunt, K. H., 1977. *Kinematic Geometry of Mechanisms*. Oxford University Press.
- [8] Ogunmolu, O., Gans, N., Jiang, S., and Gu, X., 2015. “An Image-Guided Soft Robotic Patient Positioning System for Maskless Head And Neck Cancer Radiotherapy: A Proof of Concept Study”. *Medical Physics: The International Journal of Medical Physics Research and Practice, Presented at the AAPM Meeting, Anaheim, CA*, **42**, June, pp. 3266–3266.
- [9] Ogunmolu, O. P., Gu, X., Jiang, S., and Gans, N. R., 2015. “A Real-Time, Soft Robotic Patient Positioning System for Maskless Head and Neck Cancer Radiotherapy: An Initial Investigation”. In Automation Science and Engineering (CASE), 2015 IEEE International Conference on, Gothenburg, Sweden, IEEE, pp. 1539–1545.
- [10] Ogunmolu, O. P., Gu, X., Jiang, S., and Gans, N. R., 2016. “Vision-based Control of a Soft Robot for Maskless Head and Neck Cancer Radiotherapy”. In Automation Science and Engineering (CASE), 2016 IEEE International Conference on, Fort Worth, Texas, IEEE, pp. 180–187.
- [11] Ogunmolu, O., Kulkarni, A., Tadesse, Y., Gu, X., Jiang, S., and Gans, N., 2017. “Soft-NeuroAdapt: A 3-DOF Neuro-Adaptive Patient Pose Correction System for Frameless and Maskless Cancer Radiotherapy”. In IEEE/RSJ International Conference on Intelligent Robots and Systems (IROS), Vancouver, BC, CA, IEEE, pp. 3661–3668.
- [12] Ogunmolu, O., and Wiersma, R. D. *Towards Real-Time Motion Compensation in Radio-Transparent Robotic*

- Radiation Therapy.*
- [13] Allen, J. J., Mäthger, L. M., Barbosa, A., and Hanlon, R. T., 2009. "Cuttlefish use visual cues to control three-dimensional skin papillae for camouflage". *Journal of Comparative Physiology A*, **195**(6), pp. 547–555.
 - [14] Pikul, J. H., Li, S., Bai, H., Hanlon, R. T., Cohen, I., and Shepherd, R. F., 2017. "Stretchable surfaces with programmable 3d texture morphing for synthetic camouflaging skins". *Science*, **358**(6360), pp. 210–214.
 - [15] Xia, Y., and Whitesides, G. M., 1998. "Soft lithography". *Angewandte Chemie International Edition*, **37**(5), pp. 550–575.
 - [16] Pikul, J., Cohen, I., and Shepherd, R., 2019. Stretchable surfaces with programmable texture, May 2. US Patent App. 16/161,029.
 - [17] Keall, P. J., Mageras, G. S., Balter, J. M., Emery, R. S., Forster, K. M., Jiang, S. B., Kapatoes, J. M., Low, D. A., Murphy, M. J., Murray, B. R., et al., 2006. "The Management of Respiratory Motion in Radiation Oncology Report of AAPM Task Group 76 A". *Medical physics*, **33**(10), pp. 3874–3900.
 - [18] Raaymakers, B., Lagendijk, J., Overweg, J., Kok, J., Raaijmakers, A., Kerkhof, E., Van der Put, R., Meijzing, I., Crijns, S., Benedosso, F., et al., 2009. "Integrating a 1.5 t mri scanner with a 6 mv accelerator: proof of concept". *Physics in Medicine & Biology*, **54**(12), p. N229.
 - [19] Lagendijk, J. J., Raaymakers, B. W., Raaijmakers, A. J., Overweg, J., Brown, K. J., Kerkhof, E. M., van der Put, R. W., Hårdemark, B., van Vulpen, M., and van der Heide, U. A., 2008. "Mri/linac integration". *Radiotherapy and Oncology*, **86**(1), pp. 25–29.
 - [20] Méndez Romero, A., Wunderink, W., Hussain, S. M., De Pooter, J. A., Heijmen, B. J., Nowak, P. C., Nuyttens, J. J., Brandwijk, R. P., Verhoef, C., Ijzermans, J. N., et al., 2006. "Stereotactic body radiation therapy for primary and metastatic liver tumors: a single institution phase i-ii study". *Acta oncologica*, **45**(7), pp. 831–837.
 - [21] Firouzeh, A., Higashisaka, T., Nagato, K., Cho, K., and Paik, J., 2020. "Stretchable kirigami components for composite meso-scale robots". *IEEE Robotics and Automation Letters*, **5**(2), pp. 1883–1890.
 - [22] Truby, R. L., Della Santina, C., and Rus, D., 2020. "Distributed proprioception of 3d configuration in soft, sensorized robots via deep learning". *IEEE Robotics and Automation Letters*.
 - [23] Hanlon, R. T., and Messenger, J. B., 1988. "Adaptive coloration in young cuttlefish (*sepia officinalis* l.): the morphology and development of body patterns and their relation to behaviour". *Philosophical Transactions of the Royal Society of London. B, Biological Sciences*, **320**(1200), pp. 437–487.
 - [24] Haubert, K., Drier, T., and Beebe, D., 2006. "Pdms bonding by means of a portable, low-cost corona system". *Lab on a Chip*, **6**(12), pp. 1548–1549.
 - [25] Walker, L. B., Harris, E., and Pontius, U., 1971. "Center of gravity of human head and neck". In ANATOMICAL RECORD, Vol. 169, WILEY-LISS DIV JOHN WILEY & SONS INC, 605 THIRD AVE, NEW YORK, NY 10158-0012, p. 448.
 - [26] Walker, L. B., Harris, E. H., and Pontius, U. R., 1973. Mass, volume, center of mass, and mass moment of inertia of head and head and neck of human body. Tech. rep., SAE Technical Paper.
 - [27] Clauser, C. E., McConvile, J. T., and Young, J. W., 1969. Weight, volume, and center of mass of segments of the human body. Tech. rep., Antioch Coll Yellow Springs OH.
 - [28] Belcher, A., 2017. "Patient Motion Management with 6-DOF Robotics for Frameless and Maskless Stereotactic Radiosurgery". PhD thesis, The University of Chicago.
 - [29] Liu, X., Belcher, A. H., Grelewicz, Z., and Wiersma, R. D., 2015. "Robotic stage for head motion correction in stereotactic radiosurgery". In 2015 American Control Conference (ACC), IEEE, pp. 5776–5781.
 - [30] Liu, X., and Wiersma, R. D., 2019. "Optimization based trajectory planning for real-time 6DoF robotic patient motion compensation systems". *PloS one*, **14**(1), p. e0210385.
 - [31] McNeil, D. G., 2005. "M.R.I.'s Strong Magnets Cited in Accidents". *The New York Times*, Aug, pp. A–1.
 - [32] Sedal, A., Memar, A. H., Liu, T., Menguc, Y., and Corson, N., 2020. "Design of deployable soft robots through plastic deformation of kirigami structures". *IEEE Robotics and Automation Letters*.
 - [33] Melnikov, A., Dorfmann, L., and Ogden, R. W., 2020. "Bifurcation of finitely deformed thick-walled electroelastic spherical shells subject to a radial electric field". *International Journal of Non-Linear Mechanics*, **121**, p. 103429.
 - [34] Canny, J. F., and Goldberg, K. Y., 1994. "risc" industrial robotics: recent results and open problems". In Proceedings of the 1994 IEEE international conference on robotics and automation, IEEE, pp. 1951–1958.
 - [35] Erdmann, M. A., and Mason, M. T., 1988. "An exploration of sensorless manipulation". *IEEE Journal on Robotics and Automation*, **4**(4), pp. 369–379.
 - [36] Mason, M. T., 2001. *Mechanics of robotic manipulation*. MIT press.
 - [37] Rivlin, R. S., and Saunders, D. W., 1950. "Large Elastic Deformations of Isotropic Materials. VII. Experiments on the Deformation of Rubber". *Philosophical Transactions of the Royal Society A: Mathematical, Physical and Engineering Sciences*, **243**(865), pp. 251–288.
 - [38] Mooney, M., 1940. "A theory of large elastic deformation". *Journal of applied physics*, **11**(9), pp. 582–592.
 - [39] Treloar, L. R. G., 1975. *The physics of rubber elasticity*. Oxford University Press, USA.
 - [40] Ogden, R., 1997. *Non-linear Elastic Deformations*. Dover Publications, Inc., Mineola, New York.
 - [41] Truesdell, C., and Noll, W., 1965. *The Non-Linear Field Theories of Mechanics*. Springer.
 - [42] Holzapfel, G. A., Gasser, T. C., and Ogden, R. W., 2000. "A new constitutive framework for arterial wall

- mechanics and a comparative study of material models". *Journal of elasticity and the physical science of solids*, **61**(1-3), pp. 1–48.
- [43] Fung, Y., Tong, P., and Chen, X., 2001. *Classical and computational solid mechanics*, Vol. 2. World Scientific Publishing Company.
- [44] Nguyen, V.-D., 1988. "Constructing force-closure grasps". *The International Journal of Robotics Research*, **7**(3), pp. 3–16.
- [45] Montana, D. J., 1988. "The Kinematics of Contact And Grasp". *The International Journal of Robotics Research*, **7**(3), pp. 17–32.
- [46] Spivak, M., 1979. "A Comprehensive Introduction to Differential Geometry. Vol. V. Berkeley: Publish or Perish". *Inc. XI*.
- [47] Murray, R. M., and Sastry, S., 1990. "Grasping and Manipulation using Multifingered Robot Hands.". In Proceedings of Symposia in Applied Mathematics, Vol. 41, pp. 329–335.
- [48] Kerr, J. R., 1984. "An Analysis of Multi-Fingered Hands". *International Journal of Robotics Research*(Dept. of Mechanical Engineering), pp. 3–17.

9 Acknowledgment

The author is grateful to Professor Kevin Turner for pointing out helpful reading material. A vote of thanks to Peter Bruno and Peter Szczesniak of Penn's Rapid Prototyping and Additive Manufacturing Labs for allowing use of their laser-cutting and tensile testing machines. Thanks to Michael Carman at the Penn Medicine Instrumentation shop for our many productive design discussions. Lastly, thanks to the Penn Biomedical library 3D printing staff for freely availing us of their FDM 3D printer.

A Deformation Gradient Derivation

It can be verified that the orthonormal basis vectors for (9) are

$$\mathbf{e}_r = \frac{\partial \mathbf{r}}{\partial r} / |\frac{\partial \mathbf{r}}{\partial r}| = \begin{bmatrix} \cos \theta \sin \phi \\ \sin \theta \sin \phi \\ \cos \phi \end{bmatrix}$$

$$\mathbf{e}_\phi = \frac{\partial \mathbf{r}}{\partial \phi} / |\frac{\partial \mathbf{r}}{\partial \phi}| = \begin{bmatrix} \cos \theta \cos \phi \\ \sin \theta \cos \phi \\ -\sin \phi \end{bmatrix}, \quad \mathbf{e}_\theta = \frac{\partial \mathbf{r}}{\partial \theta} / |\frac{\partial \mathbf{r}}{\partial \theta}| = \begin{bmatrix} -\sin \theta \\ \cos \theta \\ 0 \end{bmatrix}.$$

From (12), we can write

$$\mathbf{F} = \frac{\partial(\mathbf{dx}_r)}{\partial R} \mathbf{e}_r \otimes \mathbf{e}_R + \frac{1}{R} \frac{\partial}{\partial \Phi} (\mathbf{dx}_r \mathbf{e}_r) \otimes \mathbf{e}_\Phi$$

$$+ \frac{1}{R \sin \Phi} \frac{\partial(\mathbf{dx}_r \mathbf{e}_r)}{\partial \Theta} \otimes \mathbf{e}_\Theta + \frac{\partial}{\partial R} (\mathbf{dx}_\phi \mathbf{e}_\phi) \otimes \mathbf{e}_R \quad (77)$$

$$+ \frac{1}{R} \frac{\partial}{\partial \Phi} (\mathbf{dx}_\phi \mathbf{e}_\phi) \otimes \mathbf{e}_\Phi + \frac{1}{R \sin \Phi} \frac{\partial}{\partial \Theta} (\mathbf{dx}_\phi \mathbf{e}_\phi) \otimes \mathbf{e}_\Theta$$

$$+ \frac{\partial}{\partial R} (\mathbf{dx}_\theta \mathbf{e}_\theta) \otimes \mathbf{e}_R + \frac{1}{R \sin \Phi} \frac{\partial}{\partial \Theta} (\mathbf{dx}_\theta \mathbf{e}_\theta) \otimes \mathbf{e}_\Theta$$

whereupon,

$$\begin{aligned} \mathbf{F} = & \frac{\partial(\mathbf{dx}_r)}{\partial R} \mathbf{e}_r \otimes \mathbf{e}_R + \frac{1}{R \sin \Phi} \frac{\partial(\mathbf{dx}_r)}{\partial \Theta} \mathbf{e}_r \otimes \mathbf{e}_\Theta \\ & + \mathbf{dx}_r \frac{\sin \phi}{R \sin \Phi} \mathbf{e}_\Theta \otimes \mathbf{e}_\Theta + \frac{\mathbf{dx}_r}{R} \mathbf{e}_\phi \otimes \mathbf{e}_\Phi + \frac{1}{R} \frac{\partial(\mathbf{dx}_r)}{\partial \Phi} \mathbf{e}_r \otimes \mathbf{e}_\Phi \\ & + \frac{\partial(\mathbf{dx}_\phi)}{\partial R} \mathbf{e}_\phi \otimes \mathbf{e}_R - \frac{\mathbf{dx}_\phi}{R} \mathbf{e}_r \otimes \mathbf{e}_\Phi + \frac{1}{R} \frac{\partial(\mathbf{dx}_\phi)}{\partial \Phi} \mathbf{e}_\phi \otimes \mathbf{e}_\Phi \\ & + \cos \phi \frac{\mathbf{dx}_\phi}{R \sin \Phi} \mathbf{e}_\Theta \otimes \mathbf{e}_\Theta + \frac{1}{R \sin \Phi} \frac{\partial(\mathbf{dx}_\phi)}{\partial \Theta} \mathbf{e}_\phi \otimes \mathbf{e}_\Theta \\ & + \frac{\partial(\mathbf{dx}_\theta)}{\partial R} \mathbf{e}_\theta \otimes \mathbf{e}_R + \frac{1}{R} \frac{\partial(\mathbf{dx}_\theta)}{\partial \Phi} \mathbf{e}_\theta \otimes \mathbf{e}_\Phi + \frac{1}{R \sin \Phi} \times \dots \\ & \frac{\partial(\mathbf{dx}_\theta)}{\partial \Theta} \mathbf{e}_\theta \otimes \mathbf{e}_\Theta + \frac{\mathbf{dx}_\theta}{R \sin \Phi} (-\mathbf{e}_r \sin \phi - \mathbf{e}_\phi \cos \phi) \otimes \mathbf{e}_\Theta \end{aligned} \quad (78)$$

where we have made use of the chain rule, (10), together with the identities,

$$\frac{\partial \mathbf{e}_r}{\partial r} = \frac{\partial \mathbf{e}_\phi}{\partial r} = \frac{\partial \mathbf{e}_\theta}{\partial r} = \frac{\partial \mathbf{e}_\theta}{\partial \phi} = 0, \quad \frac{\partial \mathbf{e}_\phi}{\partial \phi} = -\mathbf{e}_r, \quad \frac{\partial \mathbf{e}_r}{\partial \phi} = \mathbf{e}_\phi, \quad (79)$$

$$\begin{aligned} \frac{\partial \mathbf{e}_r}{\partial \theta} &= \mathbf{e}_\theta \sin \phi, \quad \frac{\partial \mathbf{e}_\phi}{\partial \theta} = \mathbf{e}_\theta \cos \phi, \\ \frac{\partial \mathbf{e}_\theta}{\partial \theta} &= -(\mathbf{e}_r \sin \phi + \mathbf{e}_\phi \cos \phi). \end{aligned} \quad (80)$$

in carrying out the partial derivatives of (78). In matrix form, we rewrite (78) as

$$\mathbf{F} = \begin{pmatrix} \frac{\partial(\mathbf{dx}_r)}{\partial R} & \frac{\partial(\mathbf{dx}_r)}{\partial \Phi} - \frac{\mathbf{dx}_\phi}{R} \\ \frac{\partial(\mathbf{dx}_\phi)}{\partial R} & \frac{\mathbf{dx}_r}{R} + \frac{1}{R} \frac{\partial(\mathbf{dx}_\phi)}{\partial \Phi} \\ \frac{\partial(\mathbf{dx}_\theta)}{\partial R} & \frac{1}{r} \frac{\partial \mathbf{dx}_\theta}{\partial \phi} \\ & \frac{1}{R \sin \Phi} \frac{\partial(\mathbf{dx}_r)}{\partial \Theta} - \frac{\sin \phi}{R \sin \Phi} \mathbf{dx}_\Theta \\ & \frac{1}{R \sin \Phi} \frac{\partial(\mathbf{dx}_\phi)}{\partial \Theta} - \frac{\cos \phi}{R \sin \Phi} \mathbf{dx}_\Theta \\ & \frac{1}{R \sin \Phi} \left(\frac{\partial(\mathbf{dx}_\theta)}{\partial \Theta} + \cos \phi \mathbf{dx}_\phi + \sin \phi \mathbf{dx}_r \right) \end{pmatrix} \quad (81)$$

which as a result of (10), becomes

$$\mathbf{F} = \begin{pmatrix} \frac{\partial(\mathbf{dx}_r)}{\partial R} & \frac{\partial(\mathbf{dx}_r)}{\partial R\partial\Phi} - \frac{\mathbf{dx}_\phi}{R} \\ \frac{\partial(\mathbf{dx}_\phi)}{\partial R} & \frac{\mathbf{dx}_r}{R} + \frac{1}{R} \frac{\partial(\mathbf{dx}_\phi)}{\partial\Phi} \\ \frac{\partial(\mathbf{dx}_\theta)}{\partial R} & \frac{1}{r} \frac{\partial\mathbf{dx}_\theta}{\partial\phi} \\ & \frac{1}{R\sin\Phi} \frac{\partial(\mathbf{dx}_r)}{\partial\Theta} - \frac{\mathbf{dx}_\theta}{R} \\ & \frac{1}{R\sin\Phi} \frac{\partial(\mathbf{dx}_\phi)}{\partial\Theta} - \cot\phi \frac{\mathbf{dx}_\theta}{R} \\ & \frac{\mathbf{dx}_\phi}{R} \cot\phi + \frac{\mathbf{dx}_r}{R} + \frac{1}{R\sin\Phi} \frac{\partial(\mathbf{dx}_\theta)}{\partial\Theta} \end{pmatrix} \quad (82)$$

or

$$\mathbf{F} = \begin{pmatrix} \frac{R^2}{r^2} & -\frac{\phi}{R} & -\frac{\theta}{R} \\ 0 & \frac{r}{R} + \frac{1}{R} & -\frac{\theta}{R} \cot\phi \\ 0 & 0 & \frac{r}{R} + \frac{\phi}{R} \cot\phi + \frac{1}{R\sin\Phi} \end{pmatrix}. \quad (83)$$

B Robot-Load Kinetics

We now derive the overall dynamics for the elastic IAB in Eulerian form. Following (22), a point on the surface of the IAB has the following description

$$\mathbf{r} = \begin{bmatrix} \lambda \\ \phi \end{bmatrix} = \begin{bmatrix} r/R \\ \beta - \alpha \end{bmatrix} \quad (84)$$

so that the Eulerian time differentiation of \mathbf{r} yields

$$\dot{\mathbf{r}} = [\dot{\lambda}, \dot{\phi}]^T = [\dot{r}/R, -\dot{\alpha}]^T \quad (85)$$

which follows since $\dot{R} = \dot{\beta} = 0$ in the reference configuration. Similarly, we find that $\ddot{\mathbf{r}}$ is

$$\ddot{\mathbf{r}} = [\ddot{\lambda}, \ddot{\phi}]^T = [\ddot{r}/R, -\ddot{\alpha}]^T \quad (86)$$

Recall the kinetic energy form of a continuum body (§ 5)

$$T = \frac{1}{2} \rho \mathbf{v}(\mathbf{r}, t) \cdot \mathbf{v}(\mathbf{r}, t) = \frac{1}{2} \rho \|\dot{\mathbf{r}}\|^2. \quad (87)$$

Given the incompressibility of the IAB material body, the material mass density is uniform throughout the body at a configuration so that the rate of change of the body mass, ρ , vanishes.

B.1 Case I: Cauchy Elastic IAB Material Skins

Suppose we choose a Cauchy Elastic material so that the constitutive equation that governs the Cauchy stress tensor, $\boldsymbol{\sigma}$, is independent of the path of the deformation from the reference configuration but is solely a function of the state of deformation. Then, it follows that $V = 0$. We have

$$T = \frac{1}{2} \rho \|\dot{\mathbf{r}}\|^2 = \frac{1}{2} \rho (\dot{r}^2/R^2 + \dot{\alpha}^2), V = 0. \quad (88)$$

It follows that the Lagrangian is

$$L(\mathbf{r}, \dot{\mathbf{r}}) = \frac{1}{2} \rho \|\dot{\mathbf{r}}\|^2 = \frac{1}{2} \rho (\dot{r}^2/R^2 + \dot{\alpha}^2) \quad (89)$$

and the derivatives of the canonical momenta are

$$\frac{d}{dt} \frac{\partial L}{\partial \dot{r}} = \frac{d}{dt} \left(\frac{\rho \dot{r}}{R^2} \right) = \rho \left(\frac{\ddot{r}}{R^2} - 2 \frac{\dot{r}\dot{R}}{R^3} \right) \equiv \frac{\rho}{R^2} \ddot{r} \quad (90a)$$

$$\frac{d}{dt} \frac{\partial L}{\partial \dot{\alpha}} = \frac{d}{dt} \frac{\partial L}{\partial \dot{\alpha}} = \frac{d}{dt} (\rho \dot{\alpha}) = \rho \ddot{\alpha}, \quad (90b)$$

where (90a) follows from the fact that the radius is constant in the reference configuration. We therefore have the following associated generalized forces

$$\frac{\partial L}{\partial r} = 0, \frac{\partial L}{\partial R} = -\frac{\rho \dot{r}^2}{R^3} \text{ and } \frac{\partial L}{\partial \phi} = 0. \quad (91a)$$

Recalling the Euler-Lagrange equation from (51), we may write the torque that governs the j 'th IAB as (we have dropped the j 'th index)

$$\boldsymbol{\tau} = \frac{\rho \ddot{r}}{R^2} + \rho \ddot{\alpha} + \frac{\rho \dot{r}^2}{R^3} \quad (92)$$

and in matrix form for all the system of IABs, we have

$$\boldsymbol{\tau} = \underbrace{\begin{bmatrix} \rho/R^2 & 0 \\ 0 & \rho \end{bmatrix}}_{M_{ab}} \underbrace{\begin{bmatrix} \ddot{r} \\ \ddot{\alpha} \end{bmatrix}}_{\dot{\mathbf{r}}} + \underbrace{\begin{bmatrix} \dot{r} \\ \dot{\alpha} \end{bmatrix}}^T \underbrace{\begin{bmatrix} \rho/R^3 & 0 \\ 0 & 0 \end{bmatrix}}_{C_{ab}} \underbrace{\begin{bmatrix} \ddot{r} \\ \ddot{\alpha} \end{bmatrix}}_{\dot{\mathbf{r}}} \quad (93)$$

or rewritten compactly as,

$$\boldsymbol{\tau} = M_{ab}(\mathbf{r}) \ddot{\mathbf{r}} + \dot{\mathbf{r}}^T C_{ab}(\mathbf{r}, \dot{\mathbf{r}}) \ddot{\mathbf{r}} \quad (94)$$

B.2 Case II: Green Elastic IAB Material Skins

When the stress tensor depends on the strain, we have from (62), that

$$V(\mathbf{r}) = \mathbf{tr}(\boldsymbol{\sigma} \boldsymbol{\Sigma}). \quad (95)$$

The associated force on the head is now a function of the kinetic and potential energies so that we have

$$L(\mathbf{r}, \dot{\mathbf{r}}) = \frac{1}{2}\rho\|\dot{\mathbf{r}}\|^2 + \mathbf{tr}(\boldsymbol{\sigma}\dot{\mathbf{F}}) \quad (96a)$$

$$= \frac{1}{2}\rho(\dot{r}^2/R^2 + \dot{\alpha}^2) + \mathbf{tr}(\boldsymbol{\sigma}\dot{\mathbf{F}}). \quad (96b)$$

We thus have

$$L(\mathbf{r}, \dot{\mathbf{r}}) = \frac{1}{2}\rho(\dot{r}^2/R^2 + \dot{\alpha}^2) + \mathbf{tr}(\boldsymbol{\sigma}\dot{\mathbf{F}}) \quad (97)$$

Solving for the derivatives of the kinetic and potential energies as before, we have

$$\frac{d}{dt}\frac{\partial L}{\partial \dot{r}} = \frac{\rho}{R^2}\ddot{r}, \quad \frac{d}{dt}\frac{\partial L}{\partial \dot{\phi}} = \rho\ddot{\alpha} \quad (98a)$$

with the following associated generalized forces

$$\frac{\partial L}{\partial r} = -4C_2\left(\frac{2r^3}{R^5} - \frac{R}{r^3}\right) - 4C_1\left(\frac{2R^3}{r^5} - \frac{r}{R^3}\right), \quad (99a)$$

$$\text{and } \frac{\partial L}{\partial \phi} = 0. \quad (99b)$$

We can now write the torque as

$$\begin{aligned} \boldsymbol{\tau} &= \frac{\rho\ddot{r}}{R^2} + \rho\ddot{\alpha} + \frac{\rho\dot{r}^2}{R^3} + 4C_1\left(\frac{2R^3}{r^5} + \frac{r}{R^3}\right) \\ &\quad + 4C_2\left(\frac{2r^3}{R^5} + \frac{R}{r^3}\right) \end{aligned} \quad (100)$$